2021

High Speed Modulation Characteristics of Semiconductor Nanolasers and Coupled Ring Laser Systems

Chi Xu
University of Central Florida

HIGH SPEED MODULATION CHARACTERISTICS OF SEMICONDUCTOR NANOLASERS AND COUPLED RING LASER SYSTEMS

by

CHI XU
M.E. Harbin Institute of Technology, 2015
B.E. Harbin Institute of Technology, 2013

A dissertation submitted in partial fulfillment of the requirements
for the degree of Doctor of Philosophy
in the College of Optics and Photonics
at the University of Central Florida
Orlando, Florida

Spring Term
2021

Major Professor: Patrick LiKamWa

ABSTRACT

Optical communication systems require light sources that can be modulated with high speeds. However, the modulation bandwidth of laser diodes is typically limited by an intrinsic value, its relaxation resonance frequency. In order to circumvent this limitation, a number of methods have been proposed to boost the modulation speed, including optical injection locking, quantum dots lasers with large differential gain, push-pull modulation in composite lasers. This dissertation explores two new approaches for enhancing the direct modulation bandwidth of semiconductor quantum well laser diodes.

Lasers with strong spontaneous emission have been shown to exhibit a high-speed performance theoretically. It is expected that such devices should have a modulation bandwidth on the order of several GHz under a sub-mA injection current. However, so far there has not been any experimentally observed verification of such enhanced behavior. In this work, we report on the experimental characterization of the intrinsic frequency response of metal-clad nanolasers. The probed nanolaser is optically pumped and modulated, allowing the emitted signal to be detected using a high-speed photodiode at each modulation frequency. Based on this technique, the prospect of high-speed operation of nanolasers is evaluated by measuring the D-factor, which is an order of magnitude greater than that of other state-of-the-art directly modulated semiconductor lasers.

In another experiment, we demonstrate that by tuning the gain-loss contrast between two coupled identical resonators a new degree of freedom to control the modulation frequency response is obtained. An electrically pumped microring laser system with a bending radius of 50 μm is fabricated on an InAlGaAs/InP MQW material. The integrated device was observed to lase in

continuous-wave mode at room temperature with a threshold current of 27 mA. By tuning the pumping ratio between two coupled rings, our measured results clearly show a bandwidth broadening by up to 1.63 times, which matches well with laser rate equation model.

ACKNOWLEDGMENTS

First, I would like to express my great appreciation to my advisor Professor LiKamWa who support me to complete my Ph.D. program. Being a member of Multiple Quantum Well group was a rich experience for me. His great insight in research, deep knowledge, and excellent experiment expertise always inspire me in the darkest hour of research. I feel fortunate for having the opportunity of learning and practicing in his group.

I would like to express my great gratitude to my co-advisor Professor Khajavikhan who provides me support on my research project and let me get involve in her group. I am very grateful for her trust to induce me into the nanolaser project and PT-laser project. Work experience in her group is enjoyable and help me grow fast.

I would also like to thank Professor Christodoulides. I am very grateful for his knowledge and insight I gained through his guidance. Working in the Non-Hermitian Optics is a great honor for me.

I would like to thank Professor Fathpour. I am very thankful for his constructive comments and insightful guidance. His comments of my proposal provided great help on my research project.

I would like to give my thanks to my friends and colleagues: Billy, Yousef, Thamer, Jeanette, Enrique, Gisela, Ning, Yuanhang, Shengli, Jinhan, Jialei, Zheyuan, Munan, Yangyang, Caicai, and many more guys who helped me and made me spend this unforgettable time in creol with lots of fun. I also thanks to the pet friend of my roommate Biubiu who is always able to relax me at home.

I would like to express my appreciation to my family. My parents always provide me unwavering love and support through my life. I also thanks to my grandparents, aunts and uncles, and cousins.

TABLE OF CONTENTS

LIST OF FIGURES

LIST OF TABLES

LIST OF ACRONYMS

ASE	Amplified Spontaneous Emission
BCB	Benzocyclobutene
BOE	Buffer Oxide Etch
CCW	Counter-Clockwise
CW	Clockwise
DC	Direct Current
DI	Deionized
EP	Exceptional Point
EPI	Epitaxy
FEM	Finite Element Method
GRIN	Gradient-Index
HSQ	Hydrogen Silsesquioxane
LIV	Light-Current-Voltage
MCEF	Modulation Current Efficiency Factor
MQW	Multiple Quantum Well
PD	Photodetector
PECVD	Plasma Enhanced Chemical Vapor Deposition
PT	Parity Time
QW	Quantum Dot
RF	Radio Frequency
RIE	Reactive Ion Etching
SOA	Semiconductor Optical Amplifier

TE	Traverse Electric
TEM	Transverse Electromagnetic
TM	Transverse Magnetic
TMAH	Tetramethylammonium Hydroxide
VCSEL	Vertical Cavity Surface Emitting Laser
VNA	Vector Network Analyzer

CHAPTER 1 : INTRODUCTION

Optical communications exhibit advantages of higher interconnect density and lower power consumption than the electronic counterparts, making great advances in short-reach application such as intra-chip and chip-to-chip interconnects, and data swapping [1, 2]. Light sources are required a small volume, low cost, sufficient power, high energy efficiency, stability, and single mode operation [3]. Light, in optical communication systems is primarily externally modulated and directly modulated. Direct modulation exhibits easy operation and low power consumption, however, its maximum modulation bandwidth is generally limited to a value close to the relaxation resonance frequency. Many strategies have been investigated to enhance the modulation speed of a semiconductor laser. Such as injection-locking techniques [4, 5], lasers with a higher differential gain [6], and push-pull modulation of a composite-resonator laser [7-9], to name a few.

Purcell effect has been theoretically proved to boost the modulation speed of a semiconductor laser [10-12]. By designing the cavity with strong spontaneous emission rate, the modulation bandwidth can be effectively increased. For example, VCSELs, in the past few decades, have been widely developed and used in 1-100Gb/s communication systems due to their low cost, robust operation, and high performance [13, 14]. In recent years, metal-clad nanolasers have been considered as potential light sources for high-resolution imaging and high-speed communications [15-18]. Their appeal is rooted in some of their intrinsic characteristics; for example, because of the metallic shell, the mode can become fully confined within an ultra-small volume, thus enabling dense integration on chip, while the high coupling efficiency of the spontaneous emission into the

lasing mode (large β-factor) can lead to low thresholds. In addition, these lasers tend to show a sparse modal spectra and operate in a single-mode fashion due to their miniature sizes [12, 19-21]. Altogether, the combination of low power consumptions and high modulation speeds in metal-clad nanolasers may be used to effectively address some of the main challenges of optical communications where reducing energy per bit is pursued [22].

Despite the large anticipation regarding the high-speed performance of metallic nanolasers, this aspect has so far remained largely unverified experimentally. In this work, we bridge this gap by measuring the intrinsic frequency response of metallic nanolasers at low pump power levels [23-25]. To achieve this goal, we build a virtual instrument test set which performs a point-to-point measurement at discrete modulation frequencies. We then use this information to determine the response of nanolasers at higher pump levels where the speed can reach values that are beyond our measurement capabilities.

In the past decade, parity time (PT) symmetry has been proposed as a means to mold the flow of light via enhancing light-matter interactions [26-30]. Progress in this area has so far enabled new effects such as unidirectional invisibility [31-33], sensitivity enhancement at an exceptional point [34-36], and chiral mode conversion [37-39], to name a few. In this respect, recently, single mode PT-symmetric lasers have been introduced [40-43] that can potentially be used as chip-scale light sources in on-chip optical communication links. In this vein, one may question how fast such PT-symmetric lasers can be directly modulated and what role if any does the symmetry breaking point, also known as an exceptional point (EP), play in enhancing the frequency response.

In this work, we first theoretically analyze the dynamical characteristics of a coupled microring laser. We discuss the laser system operating in PT-symmetric region and non-PT-symmetric region respectively, by giving a different value of linewidth enhancement factor. The small signal modulation response is obtained by differential rate equations, which exhibit a bandwidth broadening by tuning the gain-loss contrast between two coupled microring cavities. Next, we design and fabricate the electrically pumped coupled microring lasers on InAlGaAs MQW EPI wafer. Our experimentally results verify the expected coupling induced bandwidth enhancement.

CHAPTER 2 : MEASURING THE FREQUENCY RESPONSE OF METALLIC NANOLASERS

2.1. Introduction to metallic nanolasers

The most advantage of metal-clad lasers is that the size of the cavity can be subwavelength, which extremely increases the integration density. For conventional lasers, the cavity size cannot be reduced smaller than wavelength due to the physical footprints and effective mode volume. For example, the diameter of a conventional VCSEL is usually in size of 10 μm [44, 45], because the cavity with a large diameter is required to confine the mode in the active region. For distributed bragg lasers, several lattice periods are necessary to obtain a high finesse of the cavity, increasing the physical size of lasers. Therefore, if the mode can be effective confined without increasing the physical size of the cavity, the subwavelength laser can be designed. The metal cladding layer is an option to achieve required mode confinement.

The metal-clad cavities can be seen as metal-coated waveguides, that the mode overlapping within the gain material and metal can be tuned by adding a dielectric “shield” layer between them. And the mode in the longitudinal direction also can be confined by a dielectric layer on both side. Therefore, the gain material is super confined by the dielectric layer as well as the metallic shield. The laser emission can be extracted from the transparent aperture.

To enhance the energy-efficient performance of a laser, how to take advantage of spontaneous emission and channel into the lasing mode are significant. From Fermi Golden Rules, the stimulated emission rate is directly related to the spontaneous emission rate. However, the spontaneous emission can be channeled into any mode supported by the cavity. Therefore, the

efficiency of spontaneous emission coupling into the stimulated emission is extremely low. To lower the threshold of a laser, one can increase the efficiency of spontaneous emission. The nanocavity can be utilized to modify the rate of spontaneous emission (Purcell factor) and ratio of lasing mode over the spontaneous emission (spontaneous emission factor β). If a cavity can channel the overall spontaneous emission in bulk to the lasing mode, the threshold is only limited by non-radioactive recombination. To evaluate the spontaneous emission rate especially in a subwavelength cavity, the Purcell factor is used [46-48]:

$$F_p = \frac{\tau_{cav}}{\tau_{bulk}} = [\frac{3Q}{4\pi^2 V}\left(\frac{\lambda}{n}\right)^3] \tag{2.1}$$

where V depicts the mode volume. It expresses the cavity enhancement of spontaneous emission rate compared with that without cavity. From Eq. (2.1), the Purcell factor can be improved by compress the modal volume. For example, a cavity with a radius of 460 nm can achieve a F = 40, and a traditional Fabry-Perot laser exhibits a F at unity [49].

To achieve a high utilization of spontaneous emission, the efficiency of spontaneous emission coupling into the lasing mode also need to be considered. The spontaneous emission factor is defined by

$$\beta = \frac{F_{cav}^{(1)}}{\Sigma F_{cav}^{(k)}} \tag{2.2}$$

where the $F_{cav}^{(1)}$ is the Purcell factor of the lasing mode [50]. It can be seen as the ratio of Purcell factor of the lasing mode over those of all modes within the gain spectrum. If the laser can utilize all the spontaneous emission for lasing, the threshold is expected to be extremely low. For example,

only one cavity mode locates within the spectrum of gain medium. This factor can be simulated by putting some random dipoles in the cavity and find the radiation of the lasing mode.

The coaxial nanolaser [19] is a great candidate to achieve a thresholdless lasing performance. The idea comes from the coaxial cable used for RF signals. The fundamental mode in a coaxial cable is transverse electromagnetic (TEM) mode. And it does not have a cut-off frequency. This allows us to design a coaxial cable with a very small radius for optical modes. When considering the 3-dimensional confinement, the TEM-like mode is also supported by such coaxial cavity. Because the size of the coaxial cavities could be very small, the cavity modes can be so far away from each other that only one mode locates within the gain bandwidth. In this case, most of spontaneous emissions are channeled into the lasing mode ($\beta = 1$), leading to a subthreshold behavior in light-light curve that is smooth until saturation. The theory of thresholdless lasers is still an active area.

The inner of the cylindrical cavity is a metallic rod surrounded by a gain medium with metal cladding. The surface plasmon polariton SPP modes are supported at metal-semiconductor interface. There is a dielectric plug-in layer used to confine the photonic mode and prevent the SPP at the top and bottom interfaces. The impedance mismatch between coaxial waveguide and free space provides the resonance cavity. The laser is pumped from the air plug at the bottom aperture, and the lasing light is also collected from there. Because the modal content is extremelly sparse, by optimizing the parameters of coaxial cavity, only one photonic mode exists within the gain bandwidth.

Although the nanolaser exhibits great advantages on integration density and power consumption, some issues are still required to be solved before application in optical communication system. First, on-chip light source requires an electrically pump scheme at the room temperature. Although some efforts focus on it, we don't have an electrically pump metallic nanolaser at room temperature nowadays [51, 52]. The most challenging problem is the heat generated in the gain medium. Since the mode are super-confined by the nanocavity, the gain medium, usually the quantum wells, are deeply etched. The surface-to-volume ratio is greater than any micro-cavity. Therefore, the surface recombination rate can be extremely high. In addition, without a surrounding InP as a thermal conductor, the heat dissipation is also a big issue. These challenges limit its temperature performance. Recently, light sources at infrared using quantum dots (QDs) material are fast growing [53-55]. Due to the lateral carrier confinement of the QDs, it's not sensitive to the surface defects. And QDs laser usually exhibits a relative low threshold and stable temperature performances due to its delta function of the density of states. The nanolaser based on QDs material could be a great candidate for electrically pumped nanoscale light source [56, 57]. Another issue is the integration between the nanolasers and waveguides. Due to the mismatching of modes in nanodisk laser and rectangular waveguides, the coupling efficiency is very low.

Another research interest is the modulation speed. The relaxation resonance frequency is a function of the differential gain times the group velocity. However, if we go back to the Fermi Golden Rules, this term can be expressed by spontaneous emission terms in a sub-wavelength cavity. By miniaturizing the cavity, less cavity modes are supported and more probability of spontaneous emission coupling into the lasing mode. This predicted high-speed modulation

performance had not been experimentally verified. In the following section of this chapter, we first derive the laser rate equation for nanolasers, then express the modulation bandwidth by terms of spontaneous emission. Next, we design the metal-clad nanolaser by FEM simulation, to figure out each term of the rate equation model and evaluate the modulation bandwidth. Finally, we fabricate the optically pump nanolaser, and measure the intrinsic frequency responses.

2.2. Modes in metallic nanocavities

Modes in metallic nanocavities are similar to those in a hollow coaxial cable for RF signals, except the optical confinement in the propagating direction z. The electric and magnetic field must satisfy the Helmholtz equation:

$$\nabla^2 U + k^2 U = 0 \tag{2.3}$$

where U represents electric or magnetic field, k is the wave number. Since the cavity is a cylinder, it is easy to solve the Helmholtz equation in the cylindrical coordinates. The equation can be further deconstructed into three coordinates r, ϕ, and z, and be solved separately. The eigensolutions can be simply analyzed by considering the boundary condition. The azimuthal component and propagation component should be in harmonic forms, and the azimuthal component can be written as sine or cosine function with an integer times of ϕ. The radial component should be the first group of Bessel function, because the field value in the center of the cavity must be finite. Therefore, the solutions can be written by:

$$\Psi = J_n(k_r r)\begin{Bmatrix}\sin(n\phi)\\ \cos(n\phi)\end{Bmatrix}\exp(ik_z z) \tag{2.4}$$

where J is the first kind of Bessel function, and n is an integer. There are two kinds of solutions, depending on the field opponents on z direction. One is transverse magnetic (TM) mode, the other is transverse electric mode (TE), where the magnetic field and electric field in z direction are zero, respectively. The TM mode can be described by:

$$E_r = \frac{\partial^2 \Psi}{\partial r \partial z} \tag{2.5}$$

$$E_\phi = \frac{1}{r}\frac{\partial^2 \Psi}{\partial \phi \partial z} \tag{2.6}$$

$$E_z = (\frac{\partial^2}{\partial z^2} + k^2)\Psi \tag{2.7}$$

$$H_r = \frac{1}{r}\frac{\partial \Psi}{\partial \phi} \tag{2.8}$$

$$H_\phi = -\frac{\partial \Psi}{\partial r} \tag{2.9}$$

$$H_z = 0 \tag{2.10}$$

And the TE mode can be solved by the same method. The boundary condition of electric field gives that the $E_\phi = 0$ at $r = R$:

$$H_r = \frac{\partial^2 \Psi}{\partial r \partial z} \tag{2.11}$$

$$H_\phi = \frac{1}{r}\frac{\partial^2 \Psi}{\partial \phi \partial z} \tag{2.12}$$

$$H_z = (\frac{\partial^2}{\partial z^2} + k^2)\Psi \tag{2.13}$$

$$E_r = -\frac{1}{r}\frac{\partial \Psi}{\partial \phi} \tag{2.14}$$

$$E_\phi = -\frac{\partial \Psi}{\partial r} \tag{2.15}$$

$$E_z = 0 \tag{2.16}$$

From the boundary condition, the electric field of azimuthal component must equal to zero at semiconductor – metal interface. Therefore, the zero point of Bessel function x_n is used and the solution can be rewritten as $J_n\left(\frac{x_n r}{R}\right)[\sin(n\phi)\ or\ \cos(n\phi)]\exp(ikz)$. By shrinking the size of the cavity, the modal content can become sparse within the gain spectrum. And there is a cut-off frequency for TE and TM mode in a nanodisk structure.

As we mentioned before, the coaxial cavity structure can support another group of modes, TEM modes, which do not show a cut-off frequency. Since there is no z component of E and H, the mode solution can be found by the same way with a simple expression as:

$$\vec{E} = \frac{e^{ikz}}{r}\vec{r} \tag{2.17}$$

$$\vec{H} = \sqrt{\frac{\mu}{\varepsilon}}\frac{e^{ikz}}{r}\vec{\phi} \tag{2.18}$$

To be noticed, the above analysis is based on a condition of a perfect metal. Although some derivations exist in the practical case, this model works well for the nanolaser with a silver shield.

2.3. Nanolaser rate equations

The rate equations for a nanolaser system are given in Eqs. (2.19) and (2.20) [58]. Here, we use the relationship between the stimulated and spontaneous emission rates in order to avoid confusion arising from the treatment of group velocity in such arrangements.

$$\frac{dn_{\mathrm{c}}}{dt} = \frac{\eta_{\mathrm{i}} I}{\mathrm{q}} - \frac{F\beta}{\tau_{\mathrm{sp}} n_{\mathrm{sp}}} n_{\mathrm{p}} n_{\mathrm{c}} - \frac{F}{\tau_{\mathrm{sp}}} n_{\mathrm{c}} - \frac{n_{\mathrm{c}}}{\tau_{\mathrm{nr}}}, \tag{2.19}$$

$$\frac{dn_{\mathrm{p}}}{dt} = \frac{F\beta}{\tau_{\mathrm{sp}} n_{\mathrm{sp}}} n_{\mathrm{p}} n_{\mathrm{c}} + \frac{F\beta}{\tau_{\mathrm{sp}}} n_{\mathrm{c}} - \frac{n_{\mathrm{p}}}{\tau_{\mathrm{p}}}, \tag{2.20}$$

where n_{c} and n_{p} are the number of carrier pairs and photons respectively, η_{i} is the current injection efficiency, I is the injection current, q is the elementary charge, τ_{p} is the photon lifetime, τ_{sp} and τ_{nr} are the multiple quantum wells (MQW) spontaneous and non-radiative recombination lifetimes, respectively. The population inversion factor is defined as $n_{\mathrm{sp}} = f_{\mathrm{c}}(1 - f_{\mathrm{v}})/(f_{\mathrm{c}} - f_{\mathrm{v}})$, where f_{c} and f_{v} are the Fermi-Dirac functions, describing the occupation probabilities in the conduction and valence bands. The Purcell factor, F, indicates the cavity-enhanced spontaneous emission rate relative to that of the MQW material, and β is the spontaneous emission coupling factor, representing the ratio of the spontaneous emission that is coupled into the lasing mode. These parameters are described in further detail in [15, 59].

Applying the small signal analysis to the above rate equations, the frequency response of a laser can be expressed as $H(\omega) = \omega_{\mathrm{R}}^2/(\omega_{\mathrm{R}}^2 - \omega^2 + \mathrm{i}\gamma\omega)$, where ω_{R} is the relaxation resonance angular frequency and γ is the damping factor:

$$\omega_R^2 = \frac{F\beta}{\tau_{\mathrm{sp}} n_{\mathrm{sp}} \eta_0 h\nu} P_{\mathrm{out}} + \frac{F\beta}{\tau_{\mathrm{sp}} \tau_{\mathrm{p}}}, \tag{2.21}$$

$$\gamma = \frac{F\beta\tau_{\mathrm{p}}}{\tau_{\mathrm{sp}} n_{\mathrm{sp}} \eta_0 h\nu} P_{\mathrm{out}} + \frac{F}{\tau_{\mathrm{sp}}} + \frac{1}{\tau_{\mathrm{nr}}}. \tag{2.22}$$

In the above equations, the laser output power can be found as $P_{\mathrm{out}} = \eta_{\mathrm{i}} h\nu n_{\mathrm{p}}/\tau_{\mathrm{p}}$, and η_0 is the fraction of the generated power emitting out of the cavity. The 3-dB cut-off frequency ($f_{3\mathrm{dB}}$) is defined as the frequency where the magnitude of the impulse response function reaches half of its DC value, i.e. $|H(\omega)|^2 = 1/2$. When damping is weak, the cut-off frequency, $f_{3\mathrm{dB}}$, is approximately proportional to the relaxation resonance frequency, f_{R}, through $f_{3\mathrm{dB}} \approx 1.55 f_{\mathrm{R}}$. Clearly, ω_{R}^2 can be enhanced by increasing the output power or by improving the spontaneous emission rate (larger Purcell factor). The modulation bandwidth rapidly increases with pump power until it saturates due to damping effects. Given the above, the maximum applicable modulation bandwidth $f_{3\mathrm{dB-max}} = \sqrt{2}/(2\pi\tau_{\mathrm{p}})$ of a metal-clad nanolaser is estimated to be on the order of a few hundreds of GHz.

2.4. Cavity simulation and laser performance evaluation

From the above rate equations, it appears that some of the cavity related parameters (τ_{p}, *F,* and β) play pivotal roles in determining the modulation bandwidth of nanolasers. In order to quantify these parameters for a given nanolaser, we first simulate the electromagnetic properties using a Finite Element Method (FEM) tool. The structure of the metal-clad laser is schematically illustrated in Figure 2-1(a). This device is comprised of a cylindrical gain medium with a radius of $R = 760$ nm and a height of $d_2 = 200$ nm, consisting of six InGaAsP quantum wells. The gain is covered by a 50 nm SiO_2 layer that serves as a plug and also prevents the formation of plasmonic modes at that interface. A 40 nm air aperture is incorporated below the gain in order to increase

the mode confinement while also providing a means to optically pump the laser and to collect its emission. Besides this aperture, the device is entirely covered with silver, enabling an ultra-small and localized mode.

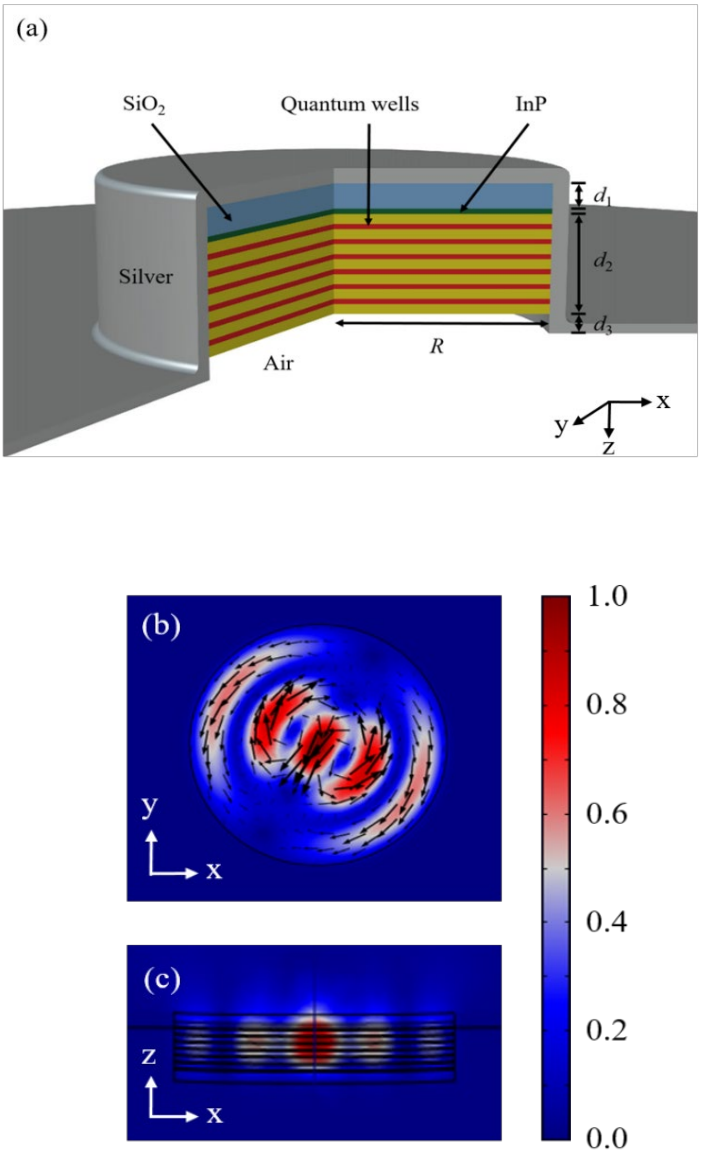

Figure 2-1 (a) The schematic of metal-clad nanolaser. (b, c) the cross-section of TE_{13} mode profile $|E|$.

The above structure is simulated using the Wave Optics module of a commercial FEM package (COMSOL Multiphysics) where the cavity modes are found by an eigenfrequency solver. Among all the possible cavity modes, we are interested only in those overlapping with the gain spectrum of the active material (InGaAsP multiple quantum wells). It is generally expected that the laser oscillations occur predominantly in the cavity modes with the highest net gain. Our simulation shows that for the structure under study, the plasmonic modes (having large radial electric field components towards the metal interface) exhibit smaller quality factors ($Q = \omega_r/2\omega_i$ for eigenfrequency $\omega = \omega_r + i\omega_i$) when compared to the photonic-type modes with electric fields predominately in the azimuthal direction. In particular, for the above nanodisk cavity, the TE_{13}-like mode shows the lowest threshold pump level when considering the lineshape of the gain system. Figure 2-1(b) and (c) display the top as well as the cross-sectional views of the normalized electric field of the TE_{13} mode. The quality factor, Q, of this mode is on the order of ~780, which results in a photon lifetime of $\tau_{\mathrm{p}} = \lambda Q/(2\pi \mathrm{c})$~0.6 ps. The Purcell factor is estimated to be $F = Q\lambda^3\xi_{\mathrm{avg}}/(4\pi^2 n^3 V_{\mathrm{eff}}) = 4.42$, where ξ_{avg} describes locations and orientations of random dipoles in relation to the modal field over the gain region, and V_{eff} is the effective cavity volume. The spontaneous emission coupling factor β is found to be 0.193, estimated by calculating the ratio of the Purcell factor of the lasing mode to the summation of the Purcell factor for all modes within the gain spectrum. The spontaneous emission lifetime for the quantum wells is $\tau_{\mathrm{sp}} = 1/(\mathrm{B}N) =$ 14.4 ns, determined by the rate equation model at steady state, where the radiative recombination coefficient B is taken as 8.9×10^{-10} cm^3/s and N is the carrier density [16].

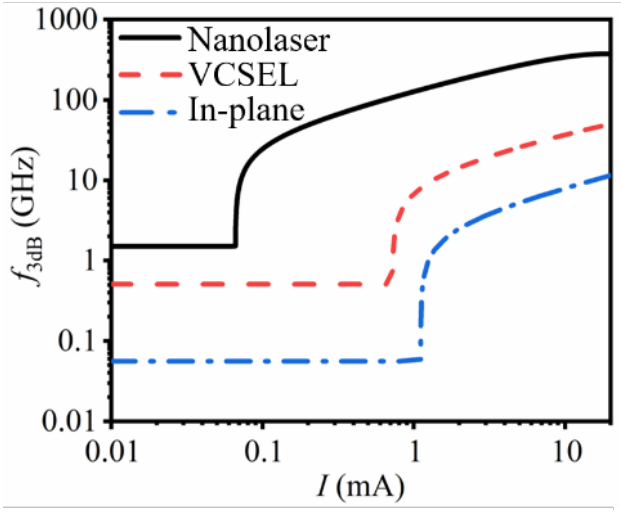

Figure 2-2 Simulated modulation bandwidths of a metallic nanolaser, a VCSEL and an in-plane laser. 3-dB bandwidth vs. injected current.

The frequency response and the modulation bandwidth of the above metallic laser can be estimated by inserting the related parameters into Eqs. (2.21) and (2.22). Figure 2-2 depicts the modulation bandwidth as a function of the injection current for a metal-clad nanolaser. This device exhibits an ultra-low threshold of $I_{\mathrm{th}} = 2\pi c n_{\mathrm{sp}} q[1 + \tau_{\mathrm{sp}}/(F\tau_{\mathrm{nr}})]/(\lambda\beta Q) \sim$ 66 μA. The modulation bandwidth $f_{3\mathrm{dB}}$ is expected to rapidly increase with the pump current until the strong damping saturates it. The maximum modulation bandwidth is found to be 374.8 GHz at I = 19.5 mA. This figure also compares the nanolaser response to that of VCSELs [60] and in-plane lasers [61]. The modulation bandwidth of the VCSEL is taken to be ~30 GHz at I = 10 mA, while most in-plane lasers show much lower speeds. The modulation current efficiency factor (MCEF), a figure of merit to compare the high-speed performance of semiconductor lasers is defined as $f_{3\mathrm{dB}}/\sqrt{I - I_{\mathrm{th}}}$. This factor is used to assess the prospect of various lasers in terms of their high-speed performance. Figure 2-3(a) shows $f_{3\mathrm{dB}}$ versus $\sqrt{I - I_{\mathrm{th}}}$ for the nanolaser, VCSEL, and in-plane laser. From this plot, an MCEF of 132 GHz/mA$^{1/2}$ can be found for the nanolaser, which is

more than ten times larger than that of VCSELs (~12.7 GHz/mA$^{1/2}$). Finally, Figure 2-3(b) displays how the relaxation resonance frequencies evolve as a function of $\sqrt{I - I_{\text{th}}}$. The slope of these curves, determines the D*-factor ($D^* = f_{\text{R}}/\sqrt{I - I_{\text{th}}}$) [62], which is found to be 86.4 GHz/mA$^{1/2}$ for the nanolaser, 8.3 GHz/mA$^{1/2}$ for the VCSEL, and 1.7 GHz/mA$^{1/2}$ for the in-plane laser.

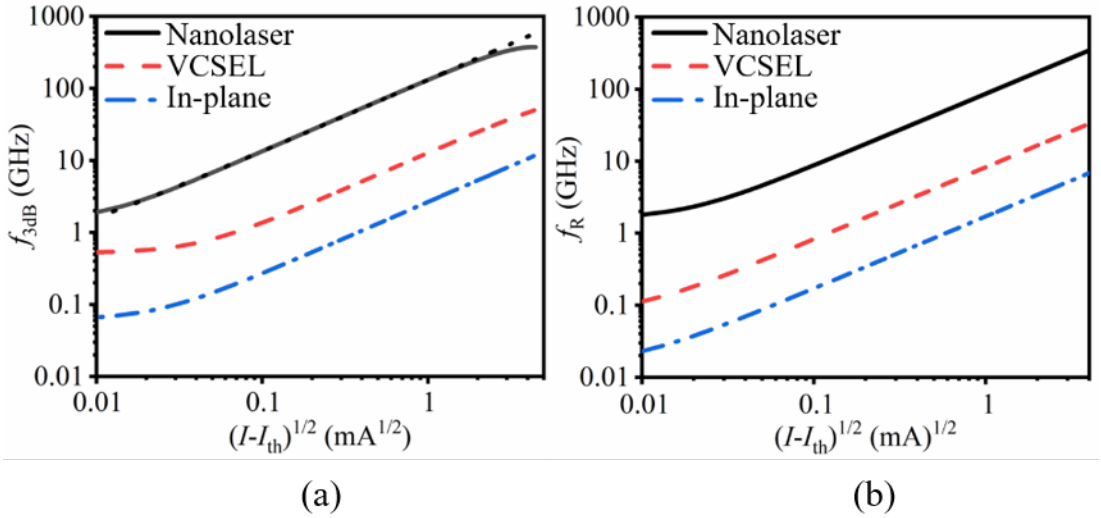

Figure 2-3 (a) 3-dB bandwidth vs. $\sqrt{I - I_{th}}$; (b) relaxation resonance frequency vs. $\sqrt{I - I_{th}}$.

2.5. Fabrication

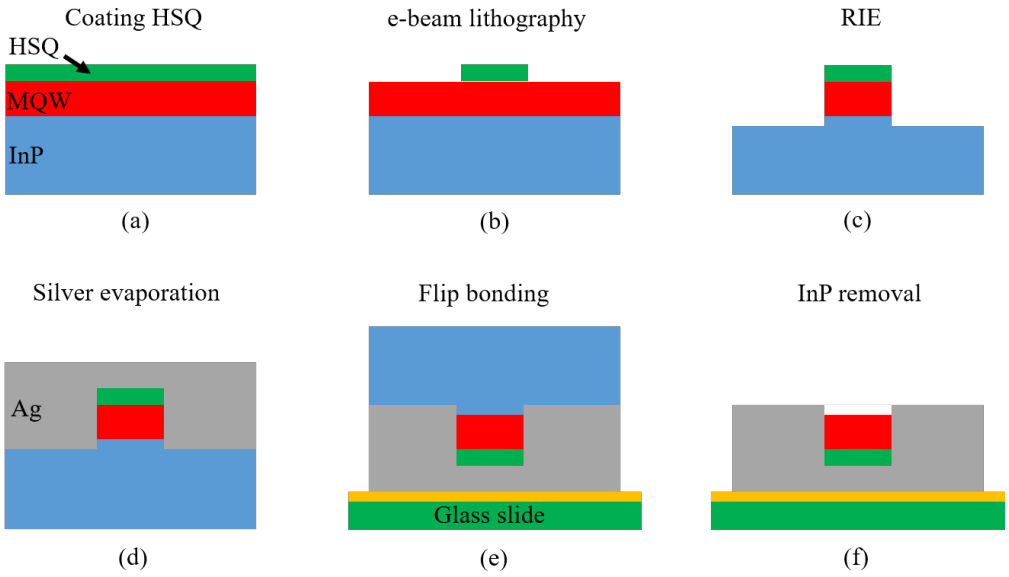

Figure 2-4 Main fabrication steps for implementing the nanolaser. (a) HSQ is spun onto the wafer; (b) the pattern is defined by means of e-beam lithography; (c) the disk structure is formed by reactive ion etching; (d) the cavities are coated with silver via e-beam deposition; (e) the wafer is flipped and bonded to a glass slide; (f) lastly the InP is removed by HCl immersion.

The fabrication steps involved in implementing the metal-clad nanolaser are depicted in Figure 2-4. The gain medium consists of 200 nm thick $In_{x=0.734}Ga_{1-x}As_{y=0.57}P_{1-y}$ (20 nm)/ $In_{x=0.56}Ga_{1-x}As_{y=0.938}P_{1-y}$ (10 nm) MQW grown on an InP substrate. On a cleaned wafer, a layer of negative electron beam resist, hydrogen silsesquioxane (HSQ) is spun. After 10 minutes of prebaking at 180°C, an EBPG 5000+ e-beam lithography system is used to write the pattern, which is then developed in tetramethylammonium hydroxide (TMAH). After exposure, the HSQ is converted to an SiO_2-like material that serves as a mask to transfer the pattern to the MQW structure by reactive ion etching (RIE) with gas proportions of H_2:CH_4:Ar = 40:4:20 SCCM. The recipe of CH_4 based dry etching is listed in Table 2-1. Since the CH_4/H_2 etching always generate polymers on the sample, especially on the mask. We run an oxygen cleaning for 5 minutes to

remove any polymer built during the RIE process. Next, a layer of silver with a thickness of 2 μm is deposited on the sample using e-beam evaporation. For mechanical handling, we flip the wafer and bond it to a glass slide. In doing so, we first spin SU-8 on top of the sample, then drop it onto a glass slide with face down. Next we exposure the SU-8 by UV for establishing the crosslink. After post-baking at 200C^{o} for 3 minutes, the sample is firmly bonded onto the glass slide. Lastly, the sample is immersed in HCl to remove the InP substrate and ready for testing.

Table 2-1 Recipe of CH_4/H_2 RIE

Chamber conditioning	10 mins
CH_4 RIE rate	50 nm/min
Temperature	20 C^{o}
Pressure	50 mTorrs
ICP power	150 W
RIE power	150 W
H_2:CH_4:Ar	40:4:20 SCCM
He cooling	10 mTorrs

2.6. Measurement station

The schematic of the test setup is shown in Figure 2-5. A 1064 nm Nd:YAG laser operating in CW mode is used to pump the metal-clad nanolaser. In addition, light generated by a 1310 nm semiconductor laser is passed through an electro-optic modulator with a 15 GHz modulation bandwidth and used as a modulation signal which is consequently amplified and polarization

corrected using a semiconductor optical amplifier (SOA) and a polarization controller (PLC). A dichroic beam splitter is used to combine the 1310 nm signal with the 1064 nm pump beam. A 50X long-working-distance objective is used to focus the pump onto and to collect the emission by the nanolasers. A polarization beam splitter (PBS) reflects the combination of pump and signal beams onto the sample and directs the output emission to the designated measurement tools. A long-pass optical filter is used to block the 1064 nm pump and 1310 nm signal from the detector. For obtaining a higher output power, the metal-clad nanolaser is inserted into a cryostat and is cooled down to 77 K using liquid nitrogen (LN_2). The laser can work at room temperature, albeit with a lower output power. However, in this measurement, we used a cooled device in order to have better signal to noise ratio. A confocal microscope scheme is used to align the nanolaser at the center of the pump beam. The laser emission with the modulated output signal is captured by a high frequency photodiode (Newport 818-BB-35) connected to an RF spectrum analyzer (HP 8560). A HP 8720 vector network analyzer (VNA) generates the RF signal which is amplified using a Mini-Circuits wideband amplifier ZVA-213+ before being applied to the electro-optic modulator. In order to measure the frequency response of the metallic nanolaser at low output powers, a virtual instrument test set is constructed. During the measurement, the response is determined point-by-point for discrete frequencies instead of directly measuring the system scattering parameter S_{21} using the vector network analyzer [23, 24, 63]. At each frequency point, the VNA generates an RF signal, while the spectrum analyzer runs a single sweep with 5 kHz range centered at this same frequency. The peak amplitude of the detected RF signal is then recorded by the control computer. The response of the nanolaser is obtained by repeating the above procedure over a range of frequencies, and normalizing the result to the system response in the

absence of the device under study. Due to the small size of the cavity, the modulated signal is relatively weak. To solve this problem, we use the above method to lower the noise floor of the RF spectrum analyzer. However, the electromagnetic interference increases at higher frequencies, limiting the capability of the measurement technique to ~9 GHz.

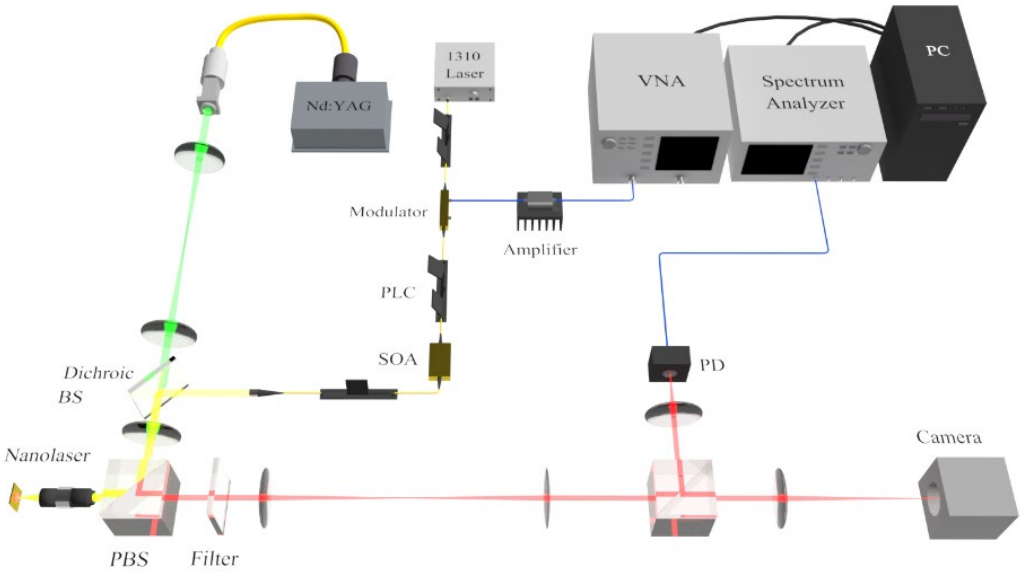

Figure 2-5 Schematic of the frequency response test setup.

2.7. Experimental result

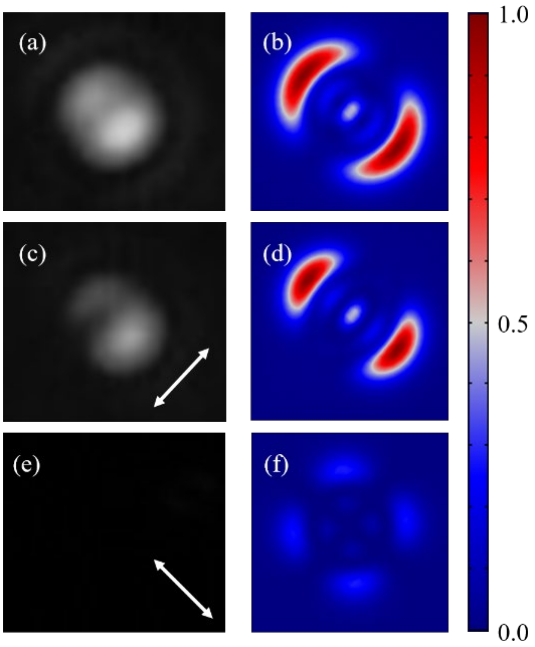

Figure 2-6 Laser characteristics. (a) Laser intensity profile; (b) Simulated normalized $|E|^2$ of the laser output; Measured (c), (e) and simulated (d), (f) orthogonal polarization components of the laser emission (the polzariation direction is indicated by the arrow). To accurately capture the emission intensity, the PBS reflecting the pump is exchanged with a non-polarizing beam splitter.

Figure 2-6(a) shows the laser output intensity profile captured by an infrared camera. Polarization resolved emission is further provided in Figure 2-6(c, e) and is compared to that of the simulated far field emission profiles of a quasi-linear TE_{13}-type mode (Figure 2-6(d, f)). This mode exhibits a great extinction ratio along two orthogonal polarization directions. Therefore, by rotating the polarizer, we find a full imaging of the mode emission and darkness on its perpendicular direction. The measured light-light curve of the metal-clad nanolaser is displayed in Figure 2-7, clearly showing a threshold pump intensity of 8 $\mu W/\mu m^2$.

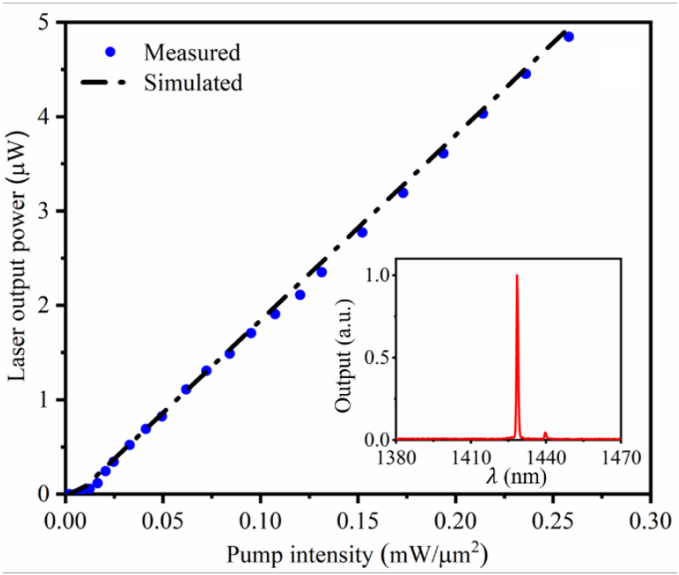

Figure 2-7 The light-light curve of the probed metallic nanolaser. Experimental results are shown as blue dots and the simulated estimation is depicted as black dashes and dots. The inset shows the lasing spectrum at a pump power level of 130 μW.

The nanolaser is operated within the linear region of the light-light curve, where the frequency response is measured in a point-by-point fashion at various output powers (Figure 2-8), as described in Section 2.6. At relatively low pump levels, the measured response exhibits the expected bandwidth broadening associated with an increasing output power (P_{out}). The characteristics of the intrinsic response f_{R}, f_{3dB}, and γ are determined by fitting the measured curves with respect to the theoretical expression $|H|^2 = f_{\mathrm{R}}^4/[f_{\mathrm{R}}^4 + f^4 - 2f_{\mathrm{R}}^2 f^2 + (\gamma f/2\pi)^2]$, shown as solid curves in Figure 2-8.

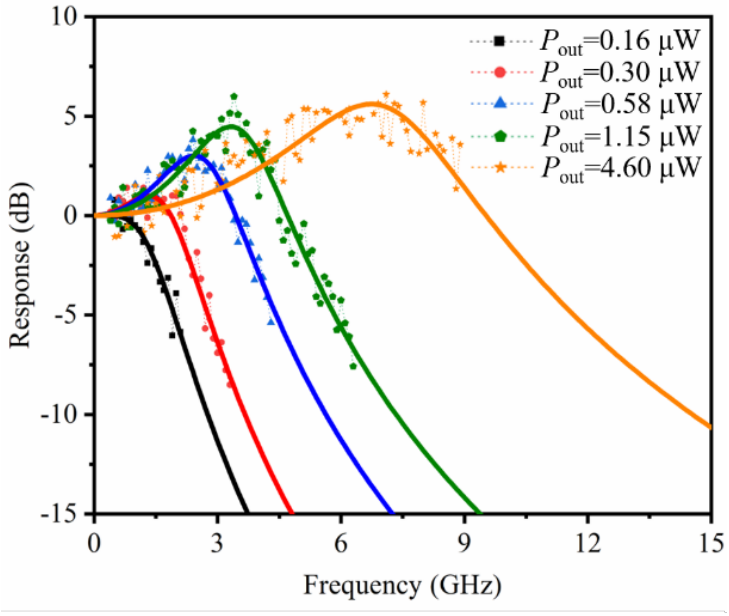

Figure 2-8 Measured frequency responses of a metallic nanolaser at various output powers.

For evaluating the high-speed performance of the nanolaser, $f_R^2\ vs.\ P_{out}$ is plotted in Figure 2-9. In addition, a simulated $f_R^2\ vs.\ P_{out}$ (dotted line) based on the above rate equation model is provided. The slope of linear fit of the experimental results is 11.6 GHz^2/μW. A figure of merit to characterize the intrinsic modulation response is the D-factor, defined as $D = f_R/\sqrt{P_{out}}$ [62]. The D-factor for the above nanolaser is found to be ~107.5 GHz/mW$^{1/2}$. To the best of our knowledge, this is the highest value reported for semiconductor lasers to date. Assuming an electrical pumping scheme with a current injection efficiency of $\eta_i = 80\%$, the MCEF estimated from the experimental results is 130 GHz/mA$^{1/2}$, which is more than an order of magnitude greater than current high speed VCSELs.

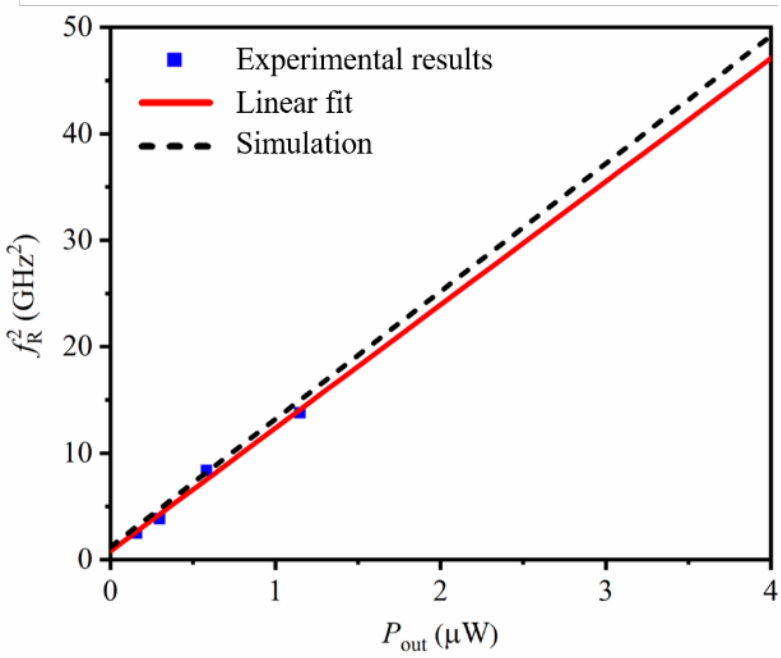

Figure 2-9 Relaxation resonance frequency squared vs. output power.

2.8. Conclusion

The intrinsic frequency response of metal-clad nanolasers has been theoretically evaluated using a rate equation model and experimentally investigated employing a point-by-point characterization method for weak signal detections. Our numerical simulation results show that the modulation bandwidth rapidly increases from its low threshold with an MCEF of 132 GHz/mA$^{1/2}$ then reaches its maximum 3-dB frequency of $f_{3\mathrm{dB-max}} = 375$ GHz. In the experiment, we measure the modulation response at relatively low pump levels (9 GHz at $P_{\mathrm{in}} = 0.25$ mW/μm^2), where we find a D-factor of 107.5 GHz/mW$^{1/2}$. This value is an order of magnitude larger than that reported for other semiconductor lasers. These exceptional features are in large attributed to the cavity enhanced spontaneous emission rate and the high β-factor, which enable high-speed

operation, even at low bias levels. We believe our results could help pave the way for designing the next generation of fast and efficient lasers.

CHAPTER 3 : THEORETICAL MODULATION CHARACTERISTICS OF COUPLED RING LASERS

3.1. Non-Hermitian optics and Parity-Time symmetric

The Hamiltonian H represents the system energy level in the quantum mechanics. In the practical condition, the energy spectrum is required to be a real value because the energy is always measurable. In addition, the energy should have a finite and stable value over the whole spectrum. This requires the energy operator Hamiltonian H to be Hermitian, which can be expressed by:

$$H = H^{\dagger}, \tag{3.1}$$

where the Hermitian operator is the combination of transposition and complex conjugation. The system has a real eigenvalue if its Hamiltonian is Hermitian [64]. For a long term, the non-Hermitian Hamiltonians have been learned to describe the system with energy dissipation. For example, the energy exponentially decays if E has an imaginary part in $\exp(iEt)$.

However, in the past decades, it was proved that the Hermiticity of Hamiltonian is not a necessary condition for a real energy spectrum [65, 66]. There are some non-Hermitian Hamiltonians presenting a real energy. This family of Hamiltonian satisfy Parity-Time symmetric, or call as space-time reflection symmetric, which can be described by:

$$H = H^{PT}, \tag{3.2}$$

where P and T represent the space-reflection and time-reflection operator, respectively. The Parity operator can flip the sign of space coordinate operator $\hat{x}$ and momentum operator $\hat{p}$.

$$P\hat{x}P = -\hat{x} \tag{3.3}$$

$$P\hat{p}P = -\hat{p} \tag{3.4}$$

And the Time-reversal operator T can reverse the sign of time, but cannot flip the sign of space coordinates:

$$T\hat{x}T = \hat{x} \tag{3.5}$$

$$P\hat{p}P = -\hat{p} \tag{3.6}$$

Also, the T operator can reverse the sign of the complex number i:

$$TiT = -i \tag{3.7}$$

P and T commute:

$$PT - TP = 0 \tag{3.8}$$

Therefore, the Hamiltonian is PT-symmetric if H commutes with PT operator:

$$H(PT) - (PT)H = 0 \tag{3.9}$$

The Schrodinger equation describes the time evolution of the wavefunction which can be written as:

$$i\frac{\partial \Psi}{\partial t} = H\Psi \tag{3.10}$$

If the potential is time-independent, H can be written as:

$$H(x) = \frac{\hat{p}}{2} + V(x) \tag{3.11}$$

where the $V(x)$ represents the potential. Since H and PT commute with each other for PT-symmetry, we can conclude the potential must satisfy:

$$V^*(-x) = V(x) \tag{3.12}$$

From Eq. (3.12), we find that the real part of potential function must be even and the imaginary part must be odd, if Hamiltonian is PT symmetric.

Recently, optics encountering PT-symmetry has received lots of research interests, because the similarity between optical wave equation and Schrodinger equation provides a simply way to exploit the phenomenon in an optical system. For example, if we write these equations in one dimensional domain, we find the refractive index can be seen as the optical potential, and energy level can be seen as the propagation constant, as shown in the following equation:

$$\left[-\frac{1}{2}\frac{\partial^2}{\partial x^2} + V(x)\right]\Psi(x) = E\Psi(x) \tag{3.13}$$

$$\left[\frac{\partial^2}{\partial x^2} + k^2 n^2(x)\right]\Psi(x) = \beta^2\Psi(x) \tag{3.14}$$

where k is $2\pi/\lambda$, and β is the propagation constant. Due to the similarity between these two equations, we can write optical potential as:

$$V(x) = -\frac{1}{2}k^2 n^2(x) \tag{3.15}$$

To be noticed, the refractive index $n(x)$ is a complex number in which the real part of index $n_{Re}(x)$ provides optical confinement, and the imaginary part $n_{Im}(x)$ provides optical gain or loss. From Eqs. (3.12) and (3.15), system Hamiltonian is PT-symmetric if $n(x)$ satisfies:

$$n_{Re}(-x) = n_{Re}(x) \tag{3.16}$$

$$n_{Im}(-x) = -n_{Im}(x) \tag{3.17}$$

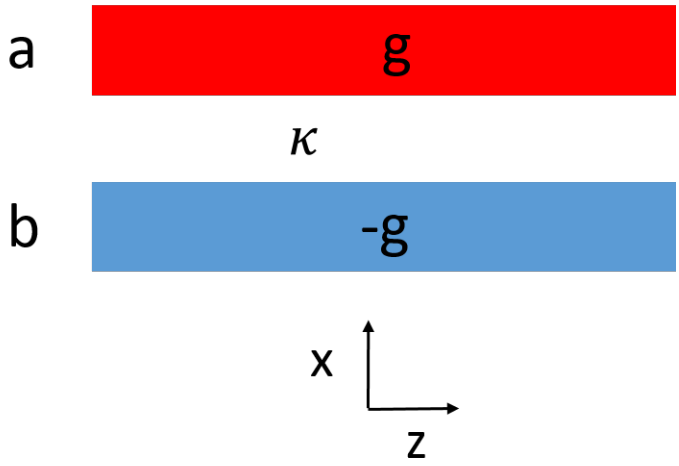

Figure 3-1 The schematic of coupled waveguides as a PT-symmetric system

These requirements can be easily achieved in optical system, since the imaginary part can be easily controlled by tuning the pumping. Considering two waveguides coupled with each other, as shown in Figure 3-1, the mode evolution between two similar waveguides can be described by coupled wave equations. Both waveguides are identical with the structure and the refractive index. Thus, the dynamics of modes are governed by:

$$i\frac{d}{dz}\begin{bmatrix} a \\ b \end{bmatrix} + \begin{bmatrix} -ig_1 & \kappa \\ \kappa & -ig_2 \end{bmatrix}\begin{bmatrix} a \\ b \end{bmatrix} = 0 \tag{3.18}$$

where a, b represent the modal field amplitudes without a time-harmonic term $\exp(-i\omega t)$, κ is the coupling coefficient. g_1 and g_2 are modal gain or loss in waveguide 1 and 2, respectively. From Eq. (3.18), the system Hamiltonian is $H = \begin{bmatrix} -ig_1 & \kappa \\ \kappa & -ig_2 \end{bmatrix}$. If H is *PT*-symmetric, g_1

requires to be equal to $-g_2$. Thus, one waveguide subjects a gain of g, and the other shows same amount of loss – g. And the Hamiltonian can be rewritten as $H = \begin{bmatrix} -ig & \kappa \\ \kappa & ig \end{bmatrix}$, where the origin of system is located in the middle of two waveguide so that $g(-x) = -g(x)$. Here we assume the carrier induced gain and loss will not affect the real refractive index. It can be achieved in a material with low linewidth enhancement factor, such as gas system and quantum dots material. By solving the equation of:

$$i\frac{d}{dz}\begin{bmatrix} a \\ b \end{bmatrix} + \begin{bmatrix} -ig & \kappa \\ \kappa & ig \end{bmatrix}\begin{bmatrix} a \\ b \end{bmatrix} = 0 \tag{3.19}$$

The solution is in the forms of $\begin{bmatrix} a \\ b \end{bmatrix} = \begin{bmatrix} a_0 \\ b_0 \end{bmatrix} e^{i\lambda z}$, which falls into two regimes. If $g < \kappa$, the eigenvalues are always real, that can be expressed as $\lambda_{1,2} = \pm\kappa\cos(\theta)$ and $\theta = \sin^{-1}(g/\kappa)$. And two eigenvectors are labeled as $|1\rangle = \begin{bmatrix} 1 \\ e^{i\theta} \end{bmatrix}$ and $|2\rangle = \begin{bmatrix} 1 \\ -e^{i\theta} \end{bmatrix}$. If $g > \kappa$, the eigenvalues are imaginary which can be written as $\lambda_{1,2} = \pm\kappa\sinh(\theta)$ and $\theta = \cosh^{-1}(g/\kappa)$. And the eigenvectors are $|1\rangle = \begin{bmatrix} 1 \\ ie^{-\theta} \end{bmatrix}$ and $|2\rangle = \begin{bmatrix} 1 \\ ie^{\theta} \end{bmatrix}$.

One interesting phenomenon is in the first regime where $g < \kappa$. The eigenvectors $|1\rangle$ and $|2\rangle$ exhibit same amplitudes along two waveguides. It implies that even if the gain-loss contrast exists between two waveguides, the supermodes are always evenly distributed in them. With the increase of coupling, this regime can be enlarged. The boundary of mode symmetry is located at $g = \kappa$, which is named as the exceptional point (EP). At this point, eigenvectors are degenerated into $|1\rangle = |2\rangle = \begin{bmatrix} 1 \\ i \end{bmatrix}$.

3.1. Rate equation modal for a laser operating in PT-broken phase

Figure 3-2 depicts a schematic of a PT-symmetric laser, comprising of a pair of identical microring resonators. The two cavities are coupled, leading to an energy exchange in time. One may also incorporate a pair of bus waveguides on either side of the rings in order to facilitate light outcoupling or extraction. The cross sections of the rings are designed in such a way so as to support the fundamental transverse electric mode (TE_{01}), which exhibits the largest overlap with the gain region. As shown in Figure 3-2, one of the resonators is subjected to gain, while the other one experiences loss (or a lower level of gain).

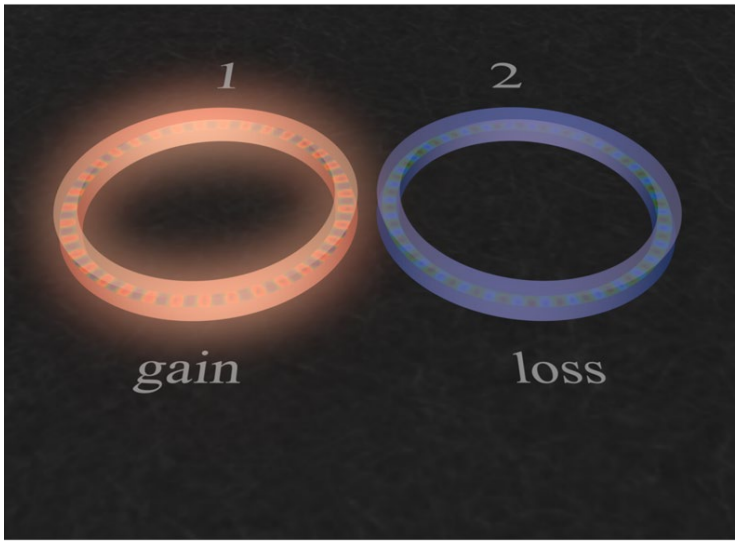

Figure 3-2 The schematic of coupled dual microring laser.

Using temporal coupled mode theory, the field amplitudes in the two resonators can be described by the following system of differential equations [67]:

$$\dot{A}_1 = -\gamma A_1 + G A_1 + j\kappa A_2, \tag{3.20}$$
$$\dot{A}_2 = -\gamma A_2 - F A_2 + j\kappa A_1, \tag{3.21}$$

where A_1, A_2 are the modal field amplitudes in the cavities with gain and loss, respectively, γ denotes the linear loss in each resonator, which is mainly due to scattering, bending and output coupling; G and F represent carrier induced gain and loss in the respective resonators, and κ is the strength of the temporal coupling coefficient.

Equations (3.20) and (3.21) support two solutions in the form of $(A_1, A_2)^T = (A_{01}, A_{02})^T \exp(-j\xi t)$, where A_{01} and A_{02} are complex constants and ξ is the eigenvalue that can be expressed as:

$$\xi = j(G - F - 2\gamma)/2 \pm \sqrt{(G + F)^2/4 - \kappa^2}. \tag{3.22}$$

Two regimes of operation can be identified, depending on whether $\delta \lessgtr 2\kappa$, where $\delta = G + F$ represents the gain-loss contrast. When $\delta < 2\kappa$, the laser operates in the unbroken PT-symmetry regime where the modal solutions of the two rings exhibit identical amplitudes and a real frequency splitting of $2\sqrt{1 - \delta^2/(4\kappa^2)}$. And the solutions are in the forms of:

$$\begin{pmatrix} a_1 \\ a_2 \end{pmatrix} = \begin{pmatrix} 1 \\ e^{\pm j\theta} \end{pmatrix} e^{(\frac{g_0 - f_0}{2} - \gamma)\tau} e^{\mp \tau \sin\theta} \tag{3.23}$$

where $g_0 = G/\kappa, f_0 = F/\kappa,$ and $\tau = \kappa t$. Here $\sin(\theta) = (g_0 + f_0)/2$. On the other hand, when $\delta > 2\kappa$, the frequency splitting occurs along the imaginary axis, and the modal amplitudes become unbalanced in terms of both amplitude and phase (displaying a $\pi/2$ phase shift). This latter situation is a characteristic of a broken PT-symmetry phase. In this case, the solution can be written as:

$$\binom{a_1}{a_2} = \binom{1}{je^{\pm\theta}} e^{(\frac{g_0 - f_0}{2} - \gamma)\tau} e^{\mp \tau \sinh\theta} \tag{3.24}$$

where $\cosh(\theta) = (g_0 + f_0)/2$. The point at which $\delta = 2\kappa$ marks the boundary between these two regimes, and is better known as an exceptional point.

Our goal here is to investigate the frequency response of PT-symmetric lasers operating in the broken phase regime. To simplify our analysis and without any loss of generality, here we consider only the interaction between the two cavities when each is emitting at a single longitudinal mode-as expected from properly designed PT-symmetric lasers operating in the broken phase. We will also assume that light circulates in each ring in a unidirectional fashion. This can be accomplished by incorporating appropriately designed S-bends in the resonators [68]. Based on these assumptions, and starting from coupled mode equations, we derive the laser rate equations in the broken PT-symmetric phase. In this regard, using Eqs. (3.20) and (3.21), one can express the modal field intensities $\left|A_{1,2}\right|^2$ in the two resonators as follows:

$$d|A_1|^2/dt = 2(G - \gamma)|A_1|^2 - 2\kappa|A_1||A_2|\sin\phi, \tag{3.25}$$

$$d|A_2|^2/dt = -2(F + \gamma)|A_2|^2 + 2\kappa|A_1||A_2|\sin\phi, \tag{3.26}$$

where ϕ is the phase shift between A_2 and A_1. In the broken PT-symmetry regime, the solution of the modal field amplitudes can be expressed as $A_2 = j\rho A_1$. At steady state, since the photons in ring 1 are expected to experience more gain, one can assign a modal ratio ρ whose value lies in the interval [0,1]. Consequently, the term representing the energy exchange between the two

cavities can be written as $2\kappa\rho|A_1|^2$, which clearly depends on the temporal coupling coefficient as well as on the modal ratio.

From Eqs. (3.25) and (3.26), one can obtain the evolution dynamics of the photon densities $S_{1,2}$, which is linearly related to the intensity of the fields in the rings ($\left|A_{1,2}\right|^2$) experiencing gain and loss. On the other hand, the carrier (N) evolution equation is considered in ring 1 and ring 2, where stimulated emission and absorption occur (in the broken phase). Under these conditions, we can express the rate equations associated with this coupled system as follows:

$$\dot{N}_1 = \eta_I I_1/(qV) - v_g g S_1 - N_1/\tau_N, \tag{3.27}$$

$$\dot{S_1} = \Gamma v_g g S_1 - S_1/\tau_p - 2\kappa sin\phi\sqrt{S_1 S_2}, \tag{3.28}$$

$$\dot{\phi} = \kappa cos\phi(1/\rho - \rho), \tag{3.29}$$

$$\dot{S_2} = -\Gamma v_g f S_2 - S_2/\tau_p + 2\kappa sin\phi\sqrt{S_1 S_2}, \tag{3.30}$$

$$\dot{N}_2 = \eta_I I_2/(qV) + v_g f S_2 - N_2/\tau_N, \tag{3.31}$$

where $I_i$is the injected current ($i = 1,2$), η_I is the current injection efficiency, q is the electron charge, V is the volume of the active region, N_i and S_i are the carrier density and photon density in each ring, respectively. v_g is the group velocity, τ_N is the carrier lifetime, and Γ is the confinement factor. g and f are the optical gain and loss per unit length, which are related to the temporal modal gain and loss coefficients G and F via $2G = \Gamma v_g g$ and $2F = \Gamma v_g f$, respectively. Finally, τ_p represents the photon lifetime which is given by $1/(2\gamma)$. Since the two cavities are identical in shape and size, Γ, τ_p and v_g are assumed to be the same for both rings.

3.2. Small signal modulation

The rate equations are now used to study the modulation frequency response function of this composite system. In this regard, we take the derivative of Eqs. (3.27) to (3.31) with respect to the variables $I_1, I_2, N_1, N_2\ S_1, S_2, \phi$. The derivative of the gain (dg) can be separated into two parts $dg = adN - a_p dN_p$, where $a = \partial g/\partial N$ and $a_p = -\partial g/\partial N_p$. We define the differential carrier lifetime $\tau_{\Delta N}$ as $1/\tau_{\Delta N} = dR_{sp}/dN + dR_{nr}/dN$. By assuming that the modulation signal is smaller than the applied bias current, one can ignore the R'_{sp}, a_p, and $\partial\alpha/\ \partial N_{\mathrm{p}}$ terms. For example, for a typical InGaAs quantum dot (QD) laser with 1mW output power, N_p is on the order of $\sim 10^{14}$ cm^{-3}, and the gain compression factor ε is around 10^{-17} cm^3 [61]. Thus, the nonlinear terms $\partial g/\partial N_p$ and $\partial\alpha/\partial N_p$ are negligible since $\varepsilon N_p \ll 1$. In addition, the term dN/dR'_{sp} is typically on the order of microseconds and can be neglected. Based on the above discussion, the differential of the rate equations can be written as:

$$(j\omega I - J)\Delta X = \eta_{\mathrm{I}}(qV)^{-1}\Delta Y \tag{3.32}$$

where $X = (N_1, S_1, \phi, S_2, N_2)$, and $Y = (I_1, 0, 0, 0, 0)$ can be expressed as $X = X_0 + \Delta X e^{j\omega t}$, $Y = Y_0 + \Delta Y e^{j\omega t}$ under the modulation. J is the Jacobian of (3.32), where each nonzero term is expressed as follows:

$$J = \begin{bmatrix} m_{NN} & m_{N1} & m_{N\phi} & m_{N2} & m_{Nn} \\ m_{1N} & m_{11} & m_{1\phi} & m_{12} & m_{1n} \\ m_{\phi N} & m_{\phi 1} & m_{\phi\phi} & m_{\phi 2} & m_{\phi n} \\ m_{2N} & m_{21} & m_{2\phi} & m_{22} & m_{2n} \\ m_{nN} & m_{n1} & m_{n\phi} & m_{n2} & m_{nn} \end{bmatrix} \tag{3.33}$$

$$m_{NN} = -1/\tau_{\Delta N} - v_g a S_1,$$

$$m_{N1} = -v_g g,$$

$$m_{1N} = m_{2n}/\rho^2 = \Gamma v_g a S_1,$$

$$m_{11} = -\kappa\rho sin\phi - 1/\tau_p + \Gamma v_g g,$$

$$m_{1\phi} = -m_{2\phi} = -2\kappa\sqrt{S_1 S_2} cos\phi,$$

$$m_{12} = -m_{21}/\rho^2 = -\kappa sin\phi/\rho,$$

$$m_{\phi 1} = -\rho^2 m_{\phi 2} = (1/S_1 + 1/S_2)\kappa\rho cos\phi/2,$$

$$m_{\phi\phi} = \kappa(\rho - 1/\rho) sin\phi,$$

$$m_{22} = -\Gamma v_g f - 1/\tau_p + \kappa sin\phi/\rho,$$

$$m_{n2} = v_g f,$$

$$m_{nn} = -1/\tau_{\Delta N} - v_g a S_2,$$

Since we assume it is a linear system under an infinite small signal modulation, each term of J can be solved under the steady state $dX/dt = 0$. In this case, g and f can be expressed by the modal ratio ρ via

$$\Gamma v_g g = 2G = 1/\tau_p + 2\kappa\rho, \tag{3.34}$$

$$\Gamma v_g f = 2F = 2\kappa/\rho - 1/\tau_p, \tag{3.35}$$

The gain-loss contrast is given by $\delta = \kappa(\rho + 1/\rho)$, that is actually controlled by unequal pumping rates. Equations (3.34) and (3.35) implies that the threshold gain g_{th} of a laser in the PT-broken symmetry regime is a function of κ through $\Gamma v_g g_{th} = 1/\tau_p + 4\kappa^2/(\Gamma v_g f + 1/\tau_p)$. As expected, for a single ring arrangement, i.e., $\kappa = 0$, $\Gamma v_g g_{th} = 1/\tau_p$. Clearly, by increasing the coupling strength κ, more photons enter into the lossy ring, and hence a higher value of gain is required in order to keep the system above threshold.

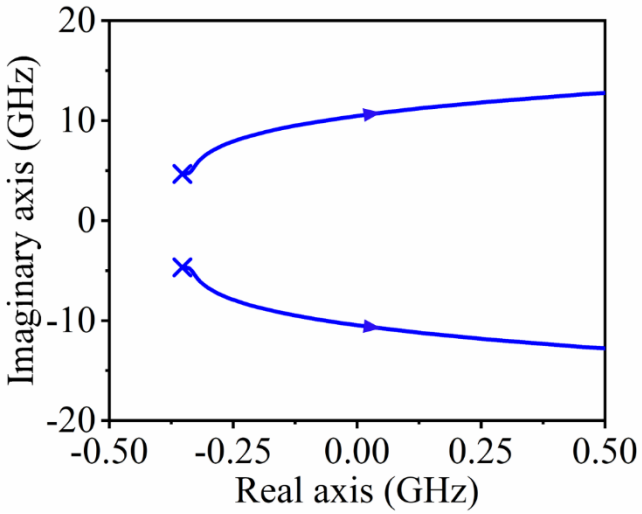

Figure 3-3 Trajectories of poles of H_1. The blue markers indicate the free running relaxation resonance frequency. The arrows show the direction of $\delta/2\kappa \to 1$ (the system approaching an EP).

The modulation frequency response $|H_1| = |\Delta S_1/\Delta I_1|$ is obtained by solving Eq. (3.32), whose characteristics depends on its zeros and poles. In contrast to a standard single cavity laser, the frequency response of a PT-symmetric laser (in the broken phase) has five poles at most. A close examination of $j\omega I - J$ reveals that, only a pair of complex-conjugate poles as a function of modal field coupling, play a pivotal role in radio frequency. This implies that the frequency

response of such a device is not only determined by the values of I, a, and τ_p, but it also depends on κ and ρ. To further visualize this new scheme of controlling the modulation characteristics, the pair of poles p of the impulse response function $H_1(j\omega)$ are depicted in Figure 3-3. The arrows show the trajectory of the poles when the system moves from a single cavity arrangement to the EP (ρ varies from 0 to 1). The poles are pulled away from free running relaxation resonance frequency (blue marks in Figure 3-3) by tuning the modal ratio, implying a bandwidth broadening mainly caused by gain-loss contrast instead of photon density.

3.3 Direct modulation bandwidth enhancement at EP

Table 3-1 The parameters of InGaAs QD lasers.

Symbol	Unit	Value
V	cm^3	1.57×10^{-12}
Γ	1	0.008
η_I	1	0.2
τ_p	ps	11
I_{th}	mA	1.8
a	cm^2	1.6×10^{-15}
$\tau_{\Delta N}$	ns	1.57
λ	nm	965
v_g	cm/s	7.1×10^9

The effect of PT-symmetry on the frequency response ($H_1(j\omega)$) of these coupled microring lasers will be further elucidated via numerical simulations. The laser parameters used in our simulations are given in Table 3-1 [69, 70], where the radius and width are 50 μm and 2 μm, respectively [61]. Figure 3-4 depicts the frequency response of a PT-symmetric laser with a coupling strength of $\kappa = 6 \times 10^{11}$ s^{-1} at a current injection level of 2 mA for various values of ρ. Compared to a single ring configuration (where $\kappa = 0$), the modulation bandwidth of the coupled ring laser broadens as ρ increases. This enhancement is attributed to the presence of an additional photon decay channel through ring 2, i.e. coupling-related term $2\kappa\rho$. Figure 3-5 displays the modulation bandwidth (f_{3dB}) in such systems as a function of $\delta/(2\kappa)$, where the system's

exceptional point occurs at $\delta/(2\kappa) = 1$. In this case, the f_{3dB} follows the square root of the injection current above threshold ($f_{3dB} \propto \sqrt{I - I_{th}}$). Therefore, the bandwidth enhancement observed in Figure 3-4 keeps independent of photon density.

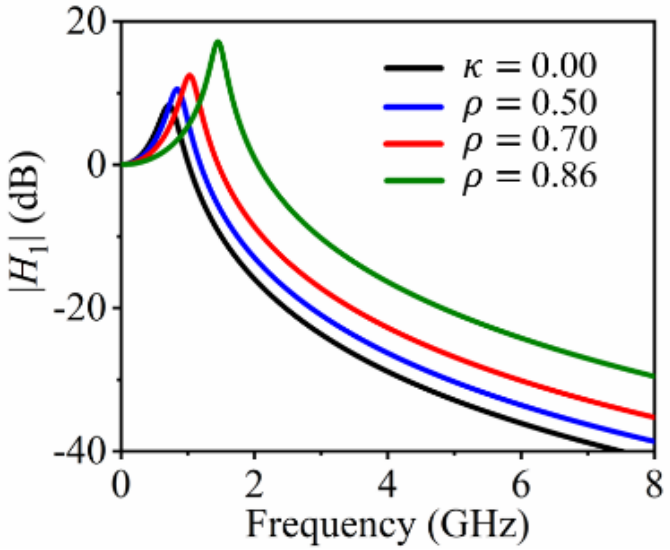

Figure 3-4 Modulation frequency responses of a PT-laser for various modal ratio.

To further understand the role of ρ in broadening the modulation bandwidth of the PT-symmetric laser, we reconsider the diagram in Figure 3-3. As indicated in the previous section, a pair of conjugate poles fashion the frequency response in RF. Others are either far away from imaginary axis or compensated with zeros. In this regard, the modulation bandwidth $f_{3dB} = 1.55|p|$ can be estimated based on the distance of one of the poles p from the origin. As shown in Figure 3-3, $|p|$ increases when the system approaches the EP, thus resulting in a broadening of the bandwidth. By considering the relaxation resonance frequency corresponding to a single cavity

configuration $\omega_R = \sqrt{\Gamma v_g a \eta_i (I - I_{th})/\mathrm{q}V}$, one can then arrive at the following expression for the 3dB cut-off frequency of a PT-symmetric laser by solving eigenvalues of Jacobian J:

$$f_{3dB-\mathrm{PT}} = \frac{f_{3dB-\mathrm{single}}}{\sqrt{1-\rho^2}}, \tag{3.36}$$

here $f_{3dB-\mathrm{single}} \approx 1.55\omega_R/(2\pi)$ is the 3dB bandwidth of the constituent ring laser. Equation (3.36) suggests a bandwidth enhancement factor of $1/\sqrt{1-\rho^2}$ for a PT-symmetric system operating in the broken regime. The enhancement is low when the gain-loss contrast is very high and increases as the system approaches the exceptional point. Beyond this point, our analysis is no longer valid since the two rings switch their functions. The dashed blue lines in Figure 3-5 depict f_{3dB} vs. $\delta/2\kappa$ from Eq. (3.36), demonstrating full agreement with the numerical solution (red solid line) for all values before the EP.

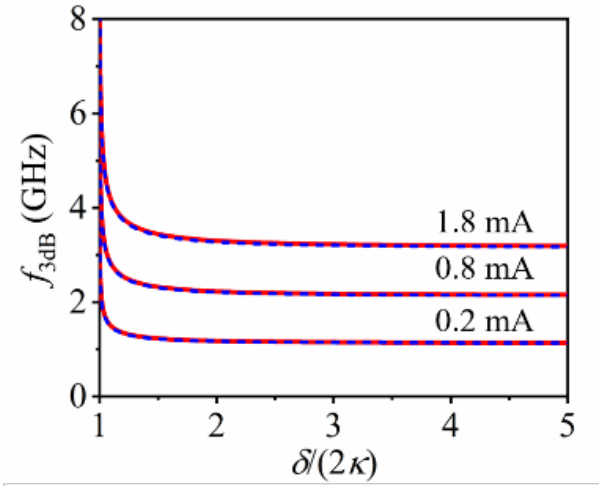

Figure 3-5 Dependences of the modulation bandwidth versus $\delta/(2\kappa)$, where the current injected above threshold $(I_1 - I_{\mathrm{th}})$ is 0.2 mA, 0.8 mA, and 1.8 mA, respectively. Red curves indicate the numerical solutions compared with estimations from Eq. (3.36) (dashed blue).

In general, the transient response of a PT-symmetric laser in the broken phase is determined by the eigenvalues Λ_i $(i = 1, 2, 3, 4, 5)$ of Jacobian J, resulting in $e^{\Lambda_i t}$ terms. The system is stable if the real components of all eigenvalues are negative; otherwise, it oscillates. An arrangement comprising only of a single ring is expected to be continuously stable since the real parts of the two poles are negative $(-\zeta/2)$, where ζ is the damping factor. However, in a PT-symmetric laser configuration, the two conjugate poles tend to move to the right-half plane when the system is approaching the exceptional point, as shown in Figure 3-3. In this case, the real part of p becomes positive after ρ reach a critical value ρ_{so} shown in Figure 3-6(a). Consequently, any small perturbation of the current will result in an oscillation that strengthens until the small signal approximation no longer applies. The effect of the injection current (I) on ρ_{so} is depicted in Figure 3-6(b). The area under each curve represents the stable region where a small signal modulation analysis holds. As shown in this figure, one can increase the stability of this system by strengthening the coupling between the two resonators. And the coupled laser system trend to stable in a relatively low pumping level.

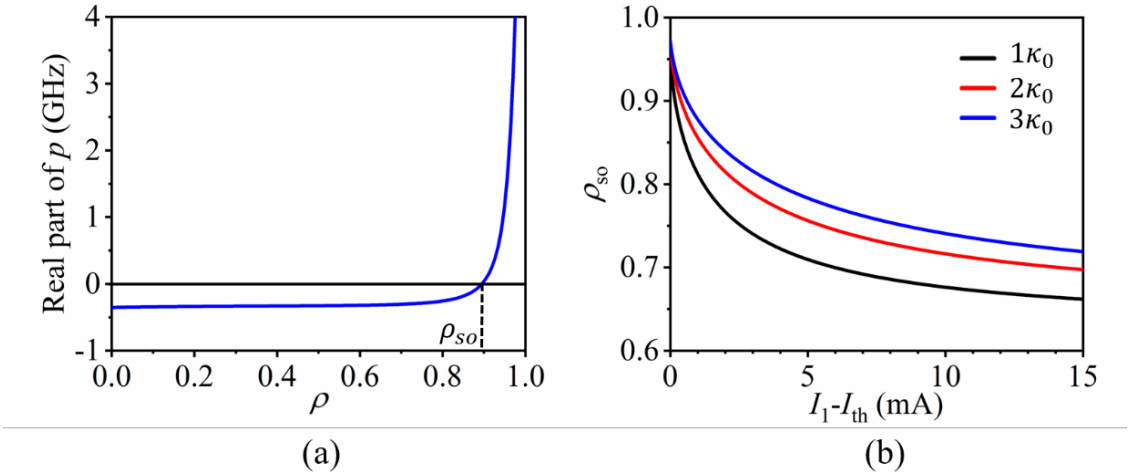

Figure 3-6 (a) The dependence of Re(p) versus ρ. ρ_{so} is the criterion of stability. The small signal modulation is stable if $\rho < \rho_{so}$. (b) Dependences of ρ_{so} versus I at different coupling coefficients κ.

3.4. Non-PT-symmetric system

In this section, we discuss the rate equation and the dynamical effects of this coupled laser system with consideration of nonzero linewidth enhancement factor α. The evanescently coupled gain-loss system is described by coupled mode equation. The system Hamiltonian is PT-symmetric necessitating a zero α-factor $H = \begin{pmatrix} -ig & \kappa \\ \kappa & ig \end{pmatrix}$. However, the gain and refractive index directly depend on carrier density in semiconductor, which leads to a great value of α. Although α can be reduced around zero in quantum dot, it cannot be ignored in most semiconductor laser. In this case, the Hamiltonian is no longer PT-symmetric:

$$H = \begin{pmatrix} -ig(1-i\alpha) & \kappa \\ \kappa & ig(1-i\alpha) \end{pmatrix} \tag{3.37}$$

We reconsider the coupled mode equation without neglecting α-factor, and obtain the rate equations expressed as follows:

$$\dot{N}_1 = \eta_I I_1/(qV) - v_g g S_1 - N_1/\tau_N, \tag{3.38}$$

$$\dot{S_1} = \Gamma v_g g S_1 - S_1/\tau_p - 2\kappa sin\phi\sqrt{S_1 S_2}, \tag{3.39}$$

$$\dot{\phi} = \alpha\Gamma v_g (g+f)/2 + \kappa cos\phi(1/\rho - \rho), \tag{3.40}$$

$$\dot{S_2} = -\Gamma v_g f S_2 - S_2/\tau_p + 2\kappa sin\phi\sqrt{S_1 S_2}, \tag{3.41}$$

$$\dot{N}_2 = \eta_I I_2/(qV) + v_g f S_2 - N_2/\tau_N, \tag{3.42}$$

where the α factor is induced in the phase equation. At steady state, $G - \gamma = \kappa\rho sin\phi$, and $F + \gamma = \kappa sin\phi/\rho$. From $d\phi/dt = 0$, we can express the phase difference as:

$$\phi = \tan^{-1}[\frac{\rho^2 - 1}{\alpha(\rho^2 + 1)}] + \pi. \tag{3.43}$$

Compared with PT-symmetry arrangement, the modal phase shifts from $\pi/2$, resulting a reduced photon decay rate through modal coupling. Therefore, it's expected that the bandwidth enhancement by pulling the resonance frequency would be reduced by a great value of α-factor. One could be curious about the frequency detuning between two rings when both rings are lasing. These frequency detuning is a common effect for a two ring resonators working as a filter. Although we assume these two rings are identical, mismatching always exists which comes from the electro-optic effect, heats, fabrication imperfections and so on. And a small amount of phase mismatching can lead to frequency detuning and loss in a coupled laser system. However, in practical application, it is hard to find these effects such as frequency splittings and increased lasing thresholds. This can be further explained by the phase dynamical term in rate equations. In

a traditional laser, phase and amplitude are not mutually coupled. Any fluctuation in phase cannot directly channel into the photon density. However, in this coupled laser system, the term $2\kappa\sin(\phi)\sqrt{S_1 S_2}$ provides a scheme for amplitude-phase coupling. If a frequency detuning occurs between two rings $\Delta\dot{\phi}$, the modal field ratio ρ varies and compensate this detuning so that the frequency detuning comes back to zero again in the steady state. Because the phase dynamic is the function of ρ, lasing always occurs on the wavelength with the smallest loss. To be noticed, the frequency detuning can occur when this coupled system is PT-symmetric. In this case, the linewidth enhancement factor is usually ignored since the coupling is very strong. And the coupling coefficient can be directly measured by Optical Spectrum Analyzer (OSA) via $\Delta\omega = 2\kappa$, where $\Delta\omega$ is the angular frequency splitting when two rings are pumped equally.

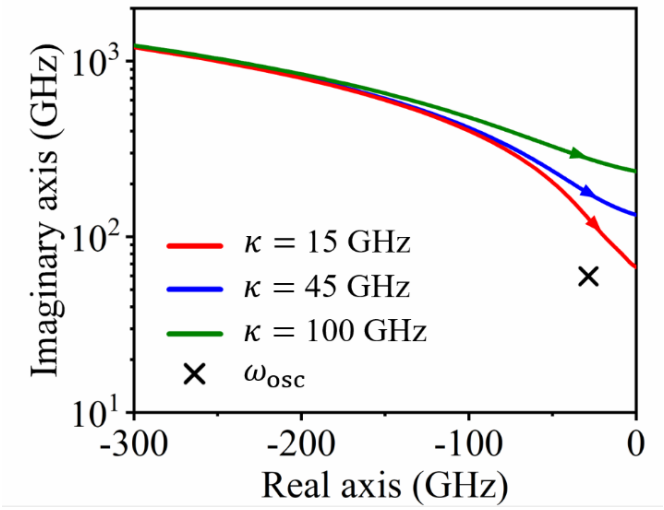

Figure 3-7 Trajectories of two characteristic poles in direction of increasing ρ (indicated by arrows), when coupling coefficient is 15 GHz, 45 GHz, and 100 GHz, respectively. Black marker indicates one pole that always locates at the oscillation frequency of the single ring laser.

The frequency response of modulating the gain cavity can be also obtained by solving Eq. (3.32), with extra nonzero terms of J ($m_{\phi N} = -m_{\phi n} = \alpha\Gamma v_g a/2$). One could notice that the

phase-amplitude coupling term ($m_{\phi 1}, m_{1\phi}, m_{\phi 2}, m_{2\phi}$) in the Jacobian is no longer zero, that could result in other zeros and poles shaping $|H_1(j\omega)|$. Therefore, we plot the trajectories of characteristic poles in RF domain when $\alpha = 4$, as shown in Figure 3-7. One is free running relaxation frequency ω_R (black mark in Figure 3-7) keeping as a invariant of κ and ρ. Solid curves of Figure 3-7 show the trajectories of the other pole p in various of ρ with different κ. With the increase of ρ (indicated by arrows in Figure 3-7), it moves rapidly towards the imaginary axis, flattening the response from ω_{R} to ω_{p}, where $\omega_{\mathrm{p}} = \mathrm{Im}(p)$. Figure 3-8 shows the normalized frequency responses of ring 1 with different κ. As expected, all curves exhibit two peaks, one at free running relaxation resonance frequency, the other around ω_{p}. The modal field ratios are optimized at $\rho = 0.23$ (red curve), and $\rho = 0.41$ (blue curve) considering stability. For a weak coupling, i.e. 15 GHz and 45 GHz, that ω_{p} is slightly greater than ω_{osc}, a roll-off beyond ω_{osc} is almost compensated by the next resonance peak. Therefore, the frequency response exhibits a broadened bandwidth with a peak in frequency response well beyond the limit of the single ring laser.

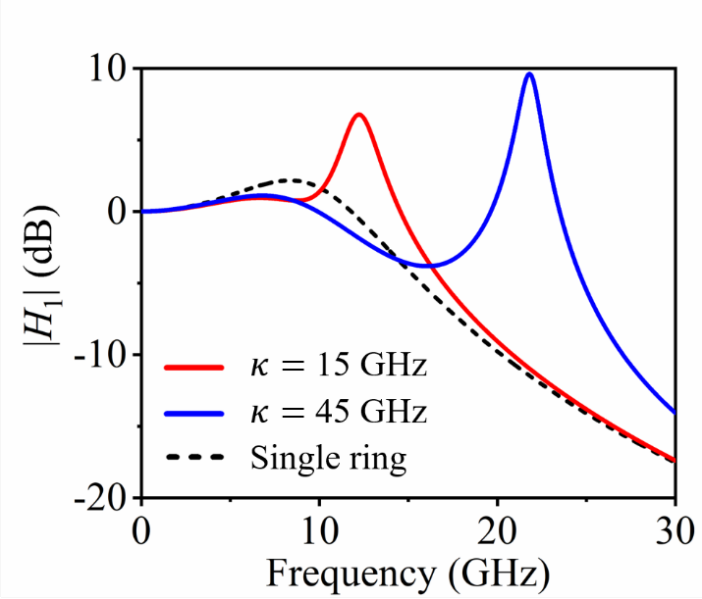

Figure 3-8 Normalized frequency responses of ring 1 with different coupling coefficients.

3.5. Conclusion

In this chapter, we have introduced a new paradigm for systematically increasing the direct modulation bandwidth of semiconductor lasers. By operating a coupled laser system in PT-broken phase, we can increase the 3-dB cut-off frequency beyond what is expected from each constituent single ring cavity by more than 2 times. This enhancement in terms of modulation bandwidth can be attributed to pulling the relaxation resonance frequency by gain-loss contrast. The resulting boost in modulation bandwidth tends to reach its highest value when the system approaches the exceptional point, which can be reached while still operating far above threshold. In a non-PT-symmetric phase, the modulation characteristics are most fashioned by phase-amplitude coupling which generates another resonance frequency in RF band. And the passband is formed between these two resonance frequency. The width of passband can be significantly broadened by

optimizing the coupling and modal ratios, which can break the limit of modulation bandwidth of each constituent ring laser.

CHAPTER 4 : ELECTRICALLY PUMPED MICRORING LASERS

4.1. Introduction

In this chapter, we design, fabricate and test the electrically pumped microring lasers based on InAlGaAs/InP MQW material. For the simplicity of design and fabrication, we first consider the ring cavity that can only support the single transverse mode TE_{01}. Without unidirectional emission, two counter-propagating modes are supported by the resonator. Due to the rotation symmetry of the ring structure, we can assume the CW mode and CCW mode are almost identical in the steady state. The scattering, reflection, and non-reciprocal effects are so small that can be ignored. We first modify the theoretical model - laser rate equations that can describe the multimode emission. Next, we numerically simulate the modulation response of microring lasers based on InAlGaAs MQW. With the optimization of coupling from the theoretical study, we design and fabricate the microring laser utilizing FEM module of Rsoft and cleanroom facilities, respectively. Finally, we characterize the laser and measure the modulation frequency responses by the network analyzer.

4.2. Laser rate equation for multimode emission

The rate equations of coupled microring lasers supporting multimodes can be described by:

$$\dot{N}_1 = \eta_I I_1/(qV) - N_1/\tau_N - \sum v_g g_m S_{1,m}, \tag{4.1}$$

$$\dot{S_{1,m}} = \Gamma v_g g_m S_{1,m} - S_{1,m}/\tau_p - 2\kappa sin\phi_m \sqrt{S_1 S_2}, \tag{4.2}$$

$$\dot{\phi_m} = \alpha\Gamma v_g (g_m + f_m)/2 + \kappa cos\phi_m (1/\rho - \rho), \tag{4.3}$$

$$\dot{S_{2,m}} = -\Gamma v_g f_m S_{2,m} - S_{2,m}/\tau_p + 2\kappa sin\phi_m \sqrt{S_{1,m} S_{2,m}}, \tag{4.4}$$

$$\dot{N}_2 = \eta_I I_2/(qV) - N_2/\tau_N + \sum v_g f_m S_{2,m}. \tag{4.5}$$

where $S_{1,m}, S_{2,m}$ are photon density of the mth mode in ring 1 and ring 2, respectively. The modes are ordered so that two modes in two cavities with the same order can mutually couple with each other. For example, in the cavity only supporting the TE_{01} mode, the CW mode in the ring 1 and CCW mode in the ring 2 are mutually coupled. Consider a ring resonator with a single transverse mode, we assume the two counter-propagating modes degenerate due to the rotation symmetry of the structure. The modulation responses of the laser system in this case, are similar to what we discuss in the previous chapter. The response $|H_1| = |\Delta S_{1,m}/\Delta I_1|$ can be obtained by applying the small signal analysis to Eqs. (4.1) to (4.5), where the parameters of the laser based on InAlGaAs MQW material are listed in Table 4-1. The simulated modulation responses of InAlGaAs MQW laser are shown in Figure 4-1. We compare the responses with the increase of gain on ring 2. The modal ratio ρ is used to describe the difference of pumping levels between two rings according to Eqs. (3.34) and (3.35). By reducing the gain-loss contrast between two rings, the modulation bandwidth increases from 2.3 GHz (single ring response shown as the black curve) to 3.7 GHz (red curve), which exhibits an enhancement of 1.6 times. This bandwidth broadening can be attributed to the appearance of the second pole, which results in a ripple in the passband. The simulation results exhibit that the coupling coefficient between two rings is an essential parameter to boost the bandwidth, which should be chosen slightly larger than the original bandwidth. In this case, κ is 5 GHz.

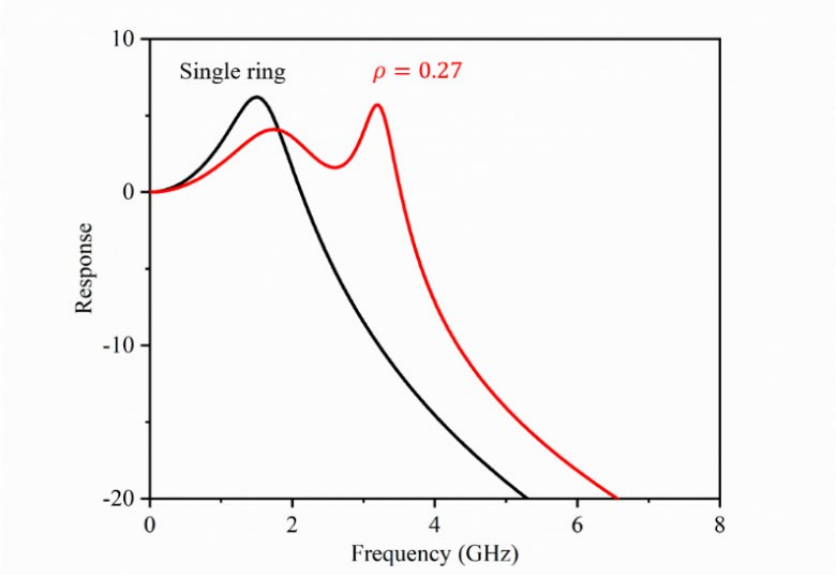

Figure 4-1 Modulation responses of InAlGaAs laser.

Table 4-1 Parameters of InAlGaAs microring lasers.

Symbol	Unit	Value
V	cm^3	4.14×10^{-11}
Γ	1	0.01
η_I	1	0.4
τ_p	ps	26
I_{th}	mA	25
a	cm^2	1.6×10^{-15}
λ	nm	1550
v_g	cm/s	9.4×10^9

4.3. InAlGaAs MQW wafer structure

The InAlGaAs/InP multiple quantum well material is used in designing microring ring lasers. The advantage of InAlGaAs MQW over that of InGaAsP MQW is the temperature performance due to it large conduction band offset ($\Delta E_c = 0.72\Delta E_g$) [71, 72]. Since the mass of an electron is small, it requires a deep barrier to confine them in the QW. The large conduction band offset of InAlGaAs MQW reduces the current leakage at a higher temperature, thus it is chosen as a desirable material for realizing microring lasers working at room temperature.

Table 4-2 InAlGaAs MQW wafer structure

P-InGaAs Layer	150 nm
P-1.5Q Layer	25 nm
P-1.3Q Layer	25 nm
P-InP	1500 nm
P-(1.1Q~1.15Q) Layer	15 nm
P-InP	50 nm
U-$In_{0.52}Al_{0.48}As$	50 nm
U-GRIN-$In_{0.53}Al_xGa_{0.47-x}As$	100 nm
QW/Barrier (λ_{PL})	5-6/9 (1508) nm
U-GRIN-$In_{0.53}Al_xGa_{0.47-x}As$	100 nm
N-$In_{0.52}Al_{0.48}As$ Layer	140 nm
N-InP Buffer Layer	500 nm
InP Substrate	

The structure of InAlGaAs MQW epitaxial wafer is shown in Table 4-2. The epitaxial layers were grown on a S doped InP substrate by metal organic chemical vapor deposition MOCVD. The intrinsic layers consist of five MQW with $\lambda_{PL} = 1508$ nm, sandwiched between two 100 nm layers of GRIN-InAlGaAs. The p type layers consist of a heavily doped InGaAs for metallization, followed by a 1.615 μm Zn doped InP cladding layer and a 100 nm InAlAs etch-stop layer. The n doped layers are compromised by a 140 nm InAlAs, followed by a 500 nm InP buffer layer.

4.4. Design and mode simulation

The ring cavity is considered at first, for realizing a large quality factor as well as the single mode operation. The finite element method FEM simulation module FemSIM of a commercial photonic simulation software Rsoft is used to find the supported modes of microring cavities. The widths of waveguides w are chosen in a range of 1-2 μm in the beginning. If the waveguide narrows less than 1 μm, the bending loss could be great due to a weak lateral confinement. And the large aspect ratio of the waveguide structure brings difficulties in the fabrication. With the increase of w, a higher order mode will be supported in the waveguide and the evanescent output coupling can by reduced dramatically. Figure 4-2 shows the fundamental mode of ring cavities with a radius of $R = 50$ μm. The quality factor is determined by $Q = n_r/2n_i$ where n_r, n_i are the real and imaginary part of refractive index. Q is large when we etch through the intrinsic layers and increases with the etching depth. n_i should be on or less than the order of 10^{-6} so that the bending loss is not the primary loss among free carrier absorptions, scatterings, and the output coupling. As shown in Figure 4-2(d), the higher order mode appears when w is larger than 2.1 μm.

In our design, we choose the width of waveguide as 1.65 μm considering the single mode operation as well as the coupling strength which will be discussed in the following section. The etching depth is chosen to be $h = 800$ nm. The bending mode in our designed structure is shown in Figure 4-2(c).

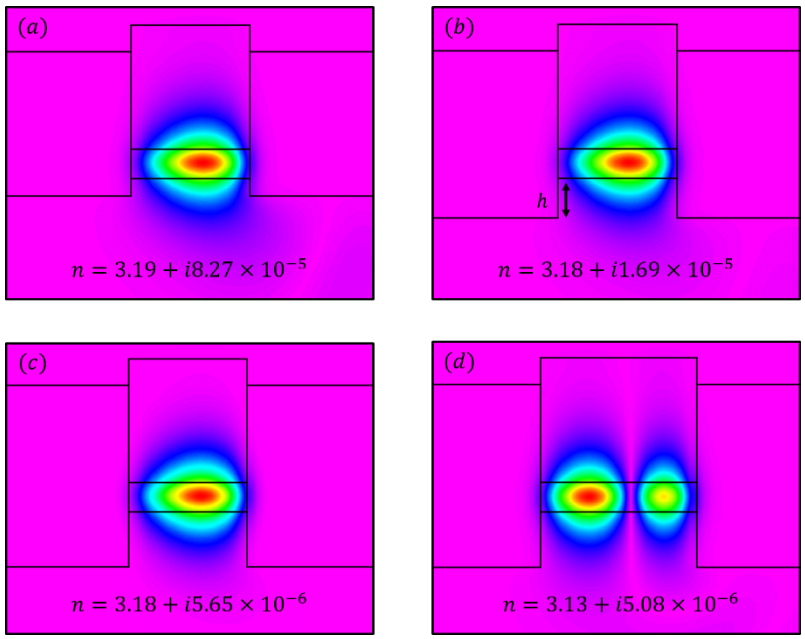

Figure 4-2 modes profile of ring cavities with a radius of 50μm in various of the etching depth and width of waveguide. (a) h=200 nm, $w = 1.65$ μm; (b) h = 500 nm, $w = 1.65$ μm; (c) h=800 nm, $w = 1.65$ μm; (d) $= h = 800$ nm, $w = 2.1$ μm.

In our design, the coupling between two ring resonators is realized by a directional coupler. Here, the temporal coupling coefficient is required to be 5 GHz which is a little bit greater than the modulation bandwidth of the ring laser. To get the temporal coupling coefficient, we first evaluate the spatial coupling coefficient of the directional coupler, then estimate the temporal coupling from the spatial one. The mode coupling in a directional coupler can be expressed by:

$$\frac{da_1}{dt} = -j\beta_1 a_1 - j\mu_{12} a_2 \tag{4.6}$$

$$\frac{da_2}{dt} = -j\beta_2 a_2 - j\mu_{21} a_1 \tag{4.7}$$

where a_i is the mode amplitude, β_i is the propagation constant, and $\mu_{i\,3-i}$ is the mutual coupling coefficient in the spatial domain. The general solution of Eqs. (4.6) and (4.7) can be in form of $a = a_0 e^{-j\beta_c z}$ and $\beta_c = (\beta_1 + \beta_2)/2 \pm \sqrt{(\beta_1 - \beta_2)^2/4 + \mu_{12}\mu_{21}}$. Due to the identity of the coupled waveguides, $\beta_1 = \beta_2$ and $\mu_{12} = \mu_{21} = \mu$. Therefore, μ can be simply expressed by $\mu = k_0 \Delta n/2$, where Δn is the difference of effective refractive index between the odd mode and even mode of the coupler.

The simulation of directional coupled is performed using the FemSIM module in Rsoft package. We use the above structure parameters of the bending waveguide while tuning the gap g between two waveguides. The coupling strength is supposed to increase exponentially by narrowing the gap. The profiles of odd and even mode in views of the waveguide cross-section are shown in Figure 4-3, where $w = 1.65$ μm, $R = 50$ μm, $h = 800$ nm, and $g = 180$ nm. And the effective refractive index of odd and even mode are $n_{odd} = 3.181146$ and $n_{even} = 3.182776$, respectively. The spatial coupling coefficient is 2.7×10^3. During one round trip, the coupling only exists in the coupling region with a distance of l_c in the spatial domain. Therefore, the temporal coupling coefficient is related to the spatial one by [73]:

$$\kappa = \frac{v_g \mu l_c}{2\pi R} \tag{4.8}$$

From Eq. (4.8), a 4.9 GHz of temporal coupling strength is obtained if the coupling distance is $l_c = 6$ μm. The coupling can be strengthened in practical due to the fabrication processes. One is

the near-field enhancement caused by the roughness of the sidewall which is formed during dry etching with high powers. The other factor is that the under etched InP in the gap due to the Aspect Ratio Dependent Etching (ARDE) reduces the confinement and increase the coupling.

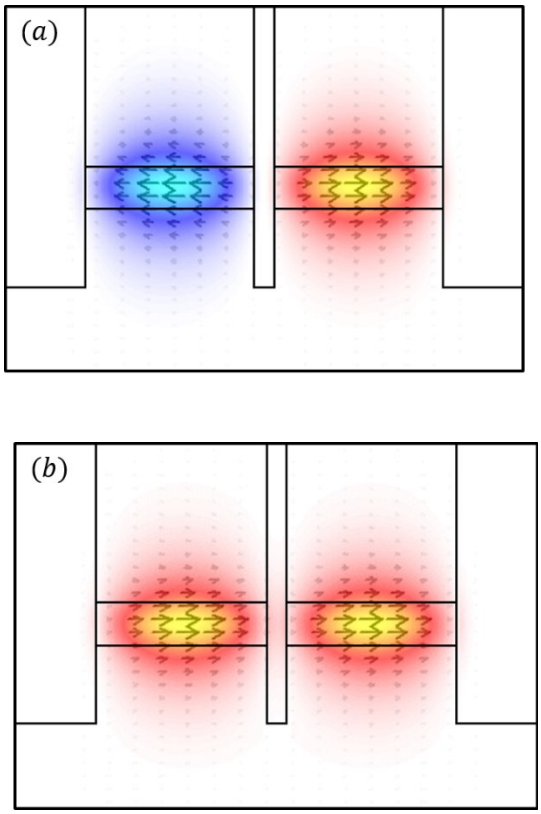

Figure 4-3 Odd (a) and even (b) modes of the directional coupler.

The output coupling is also achieved by evanescent coupling to a bus waveguide. Same simulation and optimization are done to compute the output coupling loss per round, which is $A_o = 2.6\%$ when g is chosen as 80 nm. More photons will couple into the bus waveguide if we loosen the optical confinement with a bending loss tradeoff. Considering the loss when a group of photons travel per round, the bending loss A_b is determined by:

$$A_b = 1 - e^{-4\pi R k_0 n_i} \tag{4.9}$$

which is 1.5% in our design. Other intrinsic loss coming from free carrier absorptions, scatterings, etc. can be described by a loss coefficient α_i, which is around 4 cm^{-1} from our previous measurements. The corresponding loss per around is $A_i = 1 - e^{-\alpha_i 2\pi R} = 12\%$. The output efficiency can be determined from the loss per round by:

$$\eta_o = \frac{A_o}{A_t} \tag{4.10}$$

where $A_t = 1 - (1 - A_b)(1 - A_o)(1 - A_i)$. In this case, an output efficiency of 17% is achieved in our design.

4.5. Fabrication

The fabrication procedures of electrically pumped microring lasers are shown in Figure 4-4. The sample was first ultrasonically cleaned in a bath of acetone for removing any residue, followed by soaking and rinsing with IPA and DI water. Then it was immersed into $HCl:H_3PO_4$=3:1 for 15 s to remove a 150 nm thick InP layer on top. Next the sample was spin coated with a negative tone e-beam resist FOX 16 with the recipe detailed in Table 4-3. After the e-beam lithography, the sample was first dry etched with CH_4 then etched with Cl_2. We used a combination of two etching recipes because the intrinsic layer (aluminum based) can only be etched by Cl_2 but the selectivity of Cl_2 etching is much lower than that of the CH_4.

Table 4-3 Recipe of e-beam lithography using FOX 16

Spin coating	3000 rpm
Thickness	600 nm
Pre-baking	10 mins @ 180 C^o
Exposure	450 $\mu C/cm^2$
Develop	60 s in TMAH
Post baking	10 mins @ 150 C^o

After dry etching, the roughness of sidewalls can extremely damage the laser performances like thresholds. To remove the dangling formed during the RIE, we first immersed the sample into a solution of H_3PO_4: H_2O_2: H_2O=1:1:38 for 6 seconds. Then the FOX 16 mask was removed by RIE. Next we ran a sulfide surface treatment to further smooth the etched sidewall. The sample was put in a solution of $(NH_4)_2S$ (20% in H_2O): H_2O=1: 10 in order to remove defects and form a protective monolayer to reduce the surface recombination. After 5 minutes soaking, the sample was taken out and immediately dried by N_2 without any rinsing. Then a layer of 100 nm SiO_2 was deposited on the top.

The top n-contact was first metalized on the sample, which was patterned by NR-3000PY. After development, the sample was put in RIE etcher to remove the uncovered SiO_2. Then we deposited 7 nm of Ni, followed by 20 nm of Ge and 200 nm of Au. The lift-off process was done by immersing the sample in the acetone for few minutes. BCB is used as a dielectric medium to provide a flat plane for the top p-contact and act as an insulator between electrodes. BCB was spun on the sample with 3000 rpm for 50 s. The sample was then bake in the over at 250℃ for 2 hours

to curing the BCB. The BCB is supposed to be 3 μm thick and will shrink during the high temperature processes. We ran one more cycle of BCB planarization to make sure the BCB can cover the sample. We put the sample in RTA for fusing the electrodes and stabilizing the BCB. Then we made a mask of SiO_2 with the same pattern of n-contacts on top of the BCB. After a O_2/CF_4 etching, the top n-contact will expose in the air. The BCB was further etched until the p-InGaAs layer extruded $200 - 300$ nm from BCB. The top p-contact consists of Ti/Zn/Au with a thickness of 7 nm /4 nm /500 nm deposited by thermal evaporation. The sample was then polished down to 100 μm thickness. We also deposited Ni/Ge/Au on the backside as the bottom n-contact. We ran the final step of RTA at 400℃ for 1minute to anneal the electrodes and form the ohmic contact. The sample was cleaved into slices with waveguide facets for edge emitting and mounted on a piece of copper for handling and testing.

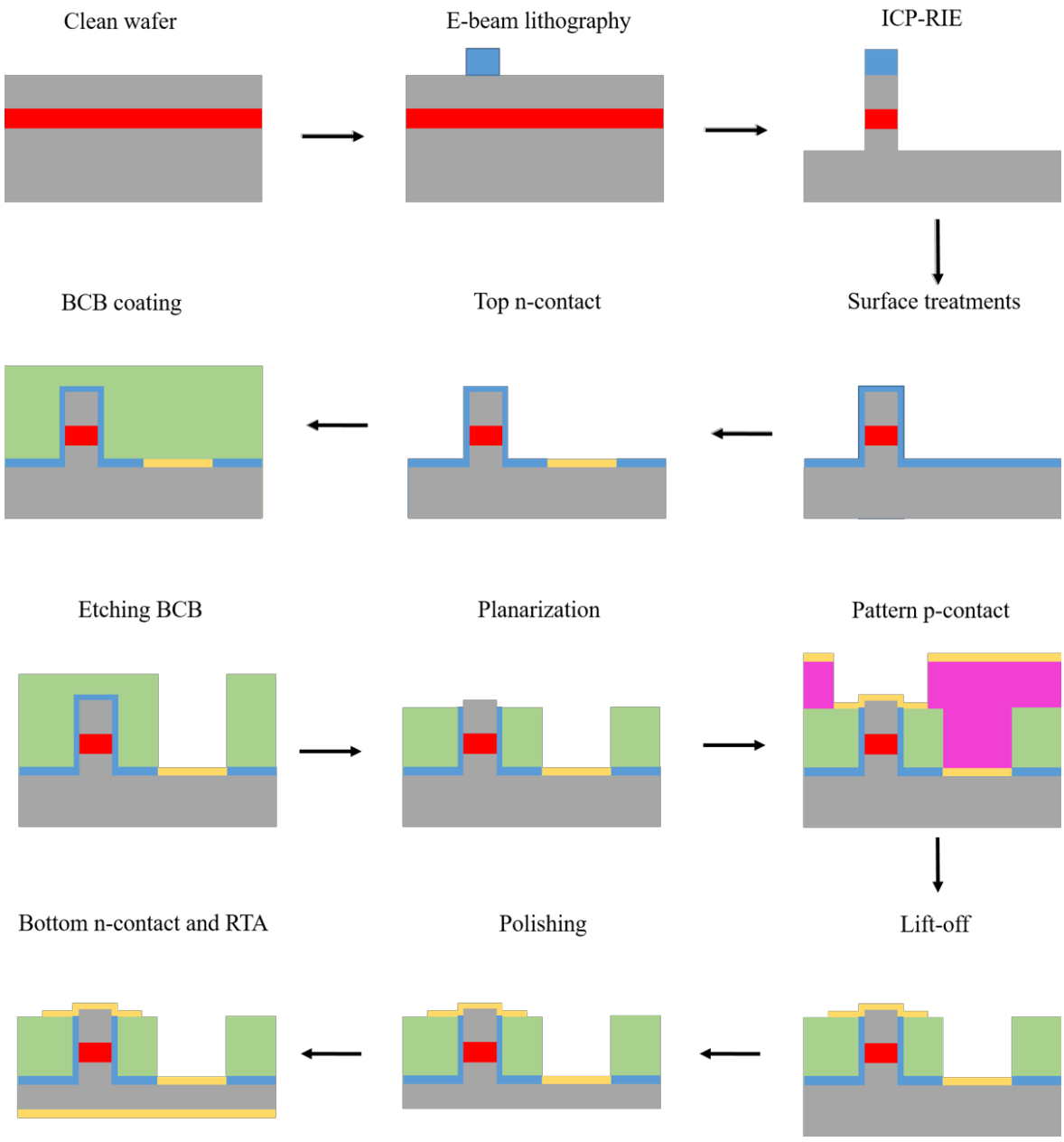

Figure 4-4 Fabrication processes of microring lasers.

4.6. Temperature performance

In the design of ring lasers, the temperature performance is an essential consideration for realizing CW operation at room temperature. Ring resonators require relative high optical confinements to reduce the bending loss, leading to a deeply etched design on waveguide structures. Although the Al based material is used to improve its temperature performance, heat can also be the most challenging problem in practical.

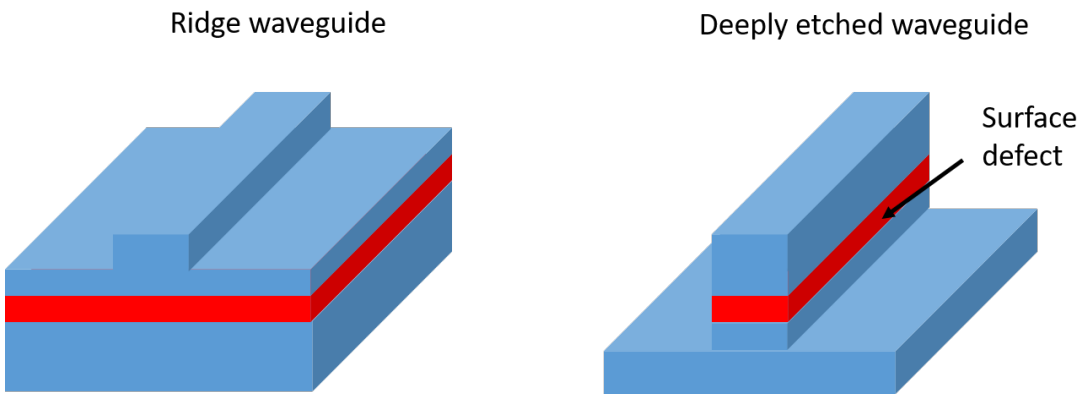

Figure 4-5 Schematics for a deeply etched waveguide and a under etched ridge waveguide

For electrically pumped schemes, semiconductor materials are used as the cladding layer, for example, the p-type InP layer with a thickness of 1.615 μm and SCH layer of 100 nm. These cladding layers also generate the heat when current is injected. And they cannot be too thin because optical modes are supposed to be isolated from the top InGaAs layer which shows a great absorption. On the other hand, for the lateral optical confinement, dielectric layers have to be used for cladding as well as planarization. Usually, BCB is chosen due to its high temperature stability, low dielectric constant for a low parasitic effect. This polymer insulates the heat dissipating into the substrate that connects to the heat sink. The thermal conductivity of BCB is around 0.3 W/mK

[74], and that of InP is 68 W/mK [75]. Therefore, the heat dissipation rate for the ridge structure is more than 10 times faster than that of the deeply etched structure. On the other hand, the use of thin film coating (SiO_2 is used for surface passivation) can also impede the heat dissipation. The thermal conductivity of thin film material is usually lower than that of the bulk material since they are amorphous due to the chemical vapor deposition process. For example, the thermal conductivity of SiO_2 is 1.1 W/mK [76], 0.7 W/mK for Si_3N_4 [77], and 5.6 for AlN. Therefore, the local temperature in the core of laser diodes can be higher than what we expect even if the thermoelectric cooler is used.

Another factor can contribute to heat and higher threshold currents is the surface recombination. The defects on the surface of the gain medium will create surface states which can trap the electrons, so that in this process electrons cannot directly recombine with holes but first drop into the surface state then drop to the valence band without a photon generation. The energy of electrons will convert into heat. This effect can extremely increase the lasing threshold and reduce the energy efficiency because it only occurs in the gain region. Since the carriers in quantum wells do not have a lateral confinement, MQW structure is sensitive to defects especially for deeply etched waveguides and nanostructures which have large surface-to-volume ratios. Nowadays the epitaxy growth techniques such as molecule beam epitaxy (MBE) and MOCVD become more and more reliable, the defects on the interface between stack layers can be ignore. Therefore, most of surface recombination occur in the sidewall surface which is a major issue for deeply etched nanostructure.

The effect of surface recombination can be characterized from *LIV* curves [78-80]. The current of a forward biased p-i-n junction can be written as:

$$I = I_1 \exp\left(\frac{qV}{kT}\right) + I_2 \exp\left(\frac{qV}{2kT}\right) \tag{4.11}$$

where *k* is the Boltzmann constant. The first term, *kT* current is usually observed at a higher biased level if we remove the voltage contributed by the load resistance. The second term, *2kT* current dominants at low pump levels, which is attributed to the surface recombination. The surface recombination current per unit length is I_s, which can be written by:

$$I_s = e s_0 L_s (np)^{1/2} \tag{4.12}$$

where *n* and *p* are densities of electrons and holes, respectively. L_s is the surface diffusion distance which can be seen as the thickness of the gain medium. s_0 is defined as the surface recombination velocity. A large value of s_0 denotes a high surface recombination rate which is directly proportional to the carrier density. Therefore, a laser diode with strong surface recombination rate can lead to a long range of 2*kT* current and a high threshold on *LIV* curves. Figure 4-6 depicts the *IV* curves of InAlGaAs MQW laser diodes with unetched MQW, deeply etched MQW, and surface passivation. The *IV* curve of the deeply etched laser shows a higher working voltages, demonstrating a higher turn-on power consumption terminating into the heat.

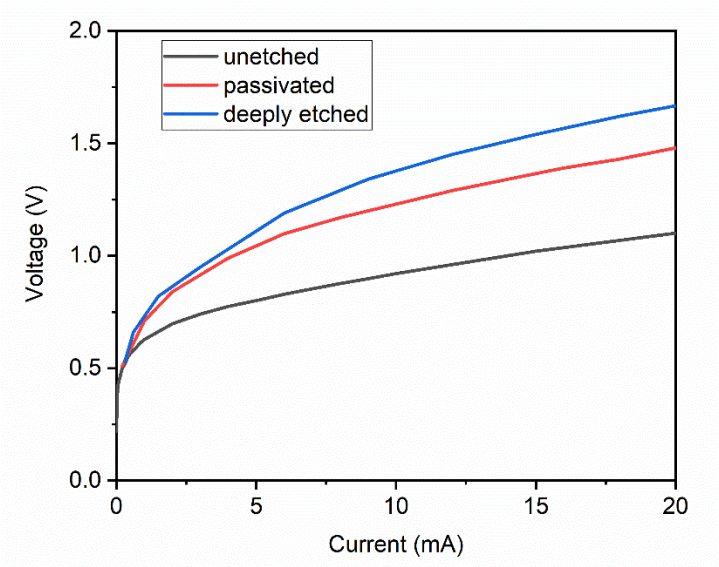

Figure 4-6 IV curves for unetched, deeply etched, surface passivated laser diodes.

One of techniques to reduce the surface recombination rate in QW or bulk materials is the surface passivation. The defects on the sidewall come from dry etching. During this process, high density plasma is generated by high power magnetic fields, and ions are hitting the surface of the sample with a high energy for obtaining an isotropic property. Therefore, dangling bonds can be created by these high energy bombarding. In order to remove these defects, we need to first clean the sidewall then passivate the etched surface. The sidewall cleaning can be done by etching the gain medium very slowly with acids. The surface passivation usually use sulfide such as ammonium sulfide or sodium sulfide for InP based materials. During this process, the etched surface can form a very thin layer of In-S bondings. The InS layer can prevent further oxidization since the In-S bonding is more stable than the In-O bonding. In addition, this passivated layer can reduce the density of surface defects. A SiO_2 coating is always followed as a protection. After the above surface treatment, threshold current can be reduced by around 4 times based on our designed laser structure.

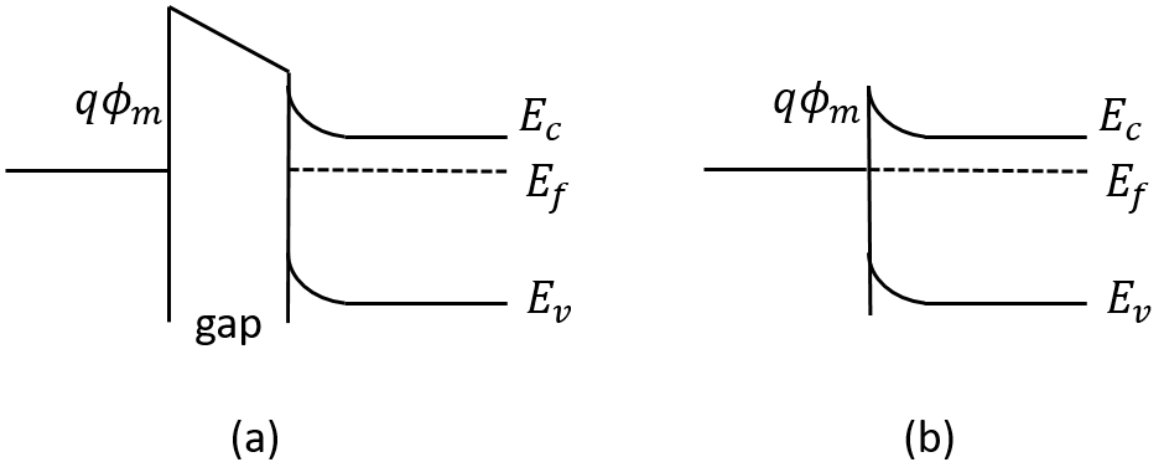

Figure 4-7 Energy-band diagrams of metal-semiconductor interfaces. (a) small gap; (b) gap is zero.

Contact resistance is one of the most important factors for electrically pumped laser diodes. The energy-band diagram is shown in Figure 4-7. As the gap between metal and semiconductor narrows, the barrier becomes thinner, and more electrons can tunnel from metal into the semiconductor. By heavily doping the semiconductor, this barrier can be further narrowed. In addition, the barrier height can be optimized by choosing metals with appropriate work functions. Zn doped $In_{0.53}Ga_{0.47}As$ is used for p-contact metallization. Metals of Ti/Zn/Au are alloyed by rapid thermal annealing around 400 ℃. Ti is used for improving the adhesion of metal contacts.

The characterization of metal contact is accomplished by transmission line measurement [81]. Considering a semiconductor material is sandwiched by two metal electrodes. The total resistance is

$$R_t = 2R_m + 2R_c + 2R_s \tag{4.13}$$

where R_m and R_s are the resistances of metal and semiconductor, respectively. R_c is the resistance of metal-semiconductor interface which is usually greater than R_m in laser diodes. If we write the semiconductor resistance in the form of sheet resistance R_{sh}, the total resistance can be expressed by:

$$R_s = R_{sh}\frac{L}{W} \tag{4.14}$$

$$R_t = 2R_{sh}\frac{L}{W} + 2R_c \tag{4.15}$$

where W is the width of pads and L is the length along the semiconductor material. If we make a series of contacts on the semiconductor with different spacing, as shown in Figure 4-8, the sheet resistance R_{sh} can be determined by the slope of $R_t - L$ lines.

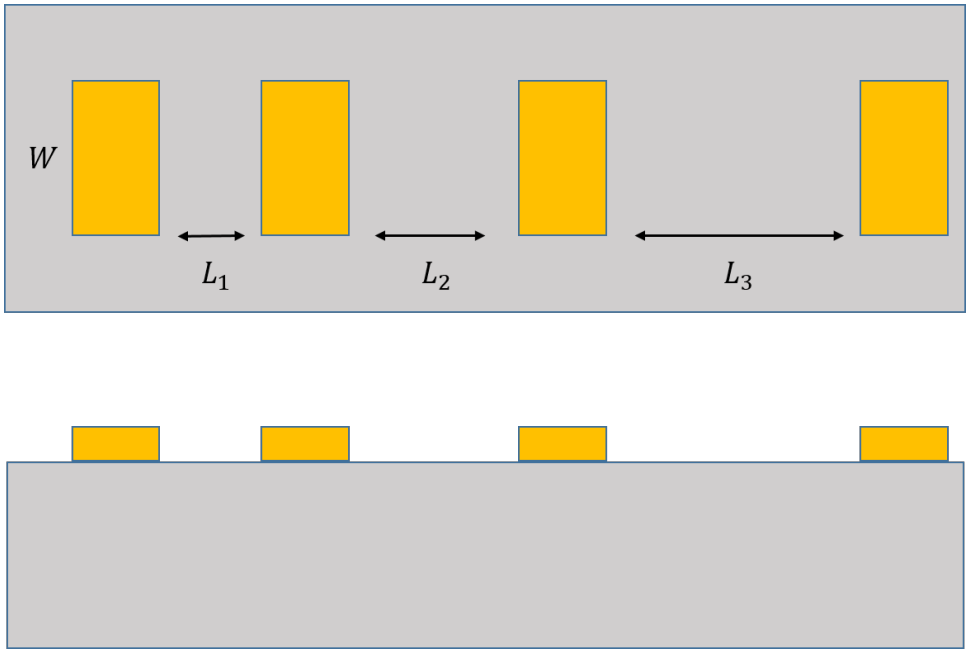

Figure 4-8 The schematic of samples for transmission line measurements.

The contact resistance can be written by resistivity ρ_c, $R_c = \rho_c/A_c$, where A_c is the contact area. However, the current flow between transmission lines is not uniform. The current density is higher at the closest boundary and lower with the increase of the distance. This effect is called the "current crowding" that the current drops exponentially with an effective length L_T, as shown in Figure 4-9. The effective length is $L_T = \sqrt{\rho_c/R_{sh}}$. Therefore, the total resistance can be written as:

$$R_t = \frac{R_{sh}}{W}(L + 2L_T) \tag{4.16}$$

The slope is R_{sh}/W and the intercept of x-axis is $-2L_T$. Then contact resistivity ρ_c can be determined.

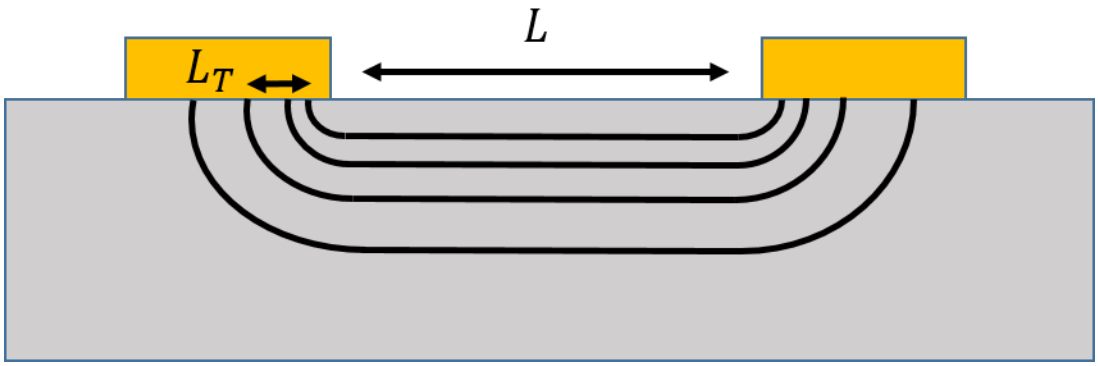

Figure 4-9 The schematic of current flow density between two electrodes.

Figure 4-10 exhibits the transmission line measurement results of the p-contact. Ti/Zn/Au = 7/4/400 nm are used, then annealed at 400 ℃ for 1 minute. The total resistances are measured by a multimeter with probes for connections, and the load resistance is characterized then removed. The red line in the figure is the linear fitting result for determining the slope and intercept. From

Figure 4-10, the sheet resistivity of semiconductor is 60 Ω, L_T is 3.35 μm, and ρ_c is $6.7 \times 10^{-6} \Omega \cdot \mathrm{cm}^2$. Therefore, the above metallization procedures exhibit a good ohm contact.

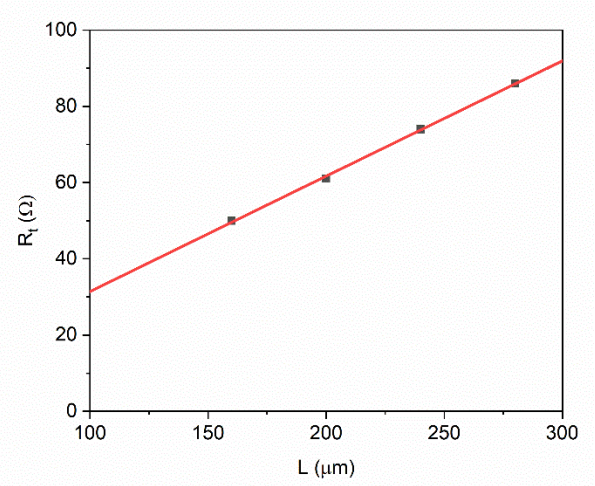

Figure 4-10 Transmission line measurement results of p-contact.

4.7. Laser characterization

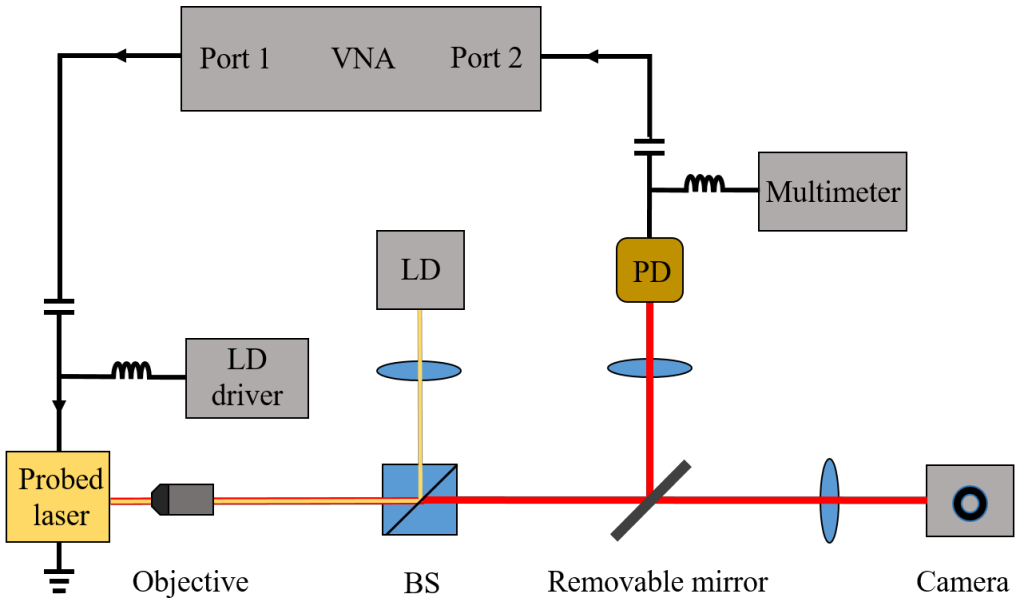

Figure 4-11 The schematic of test setup for laser characterization and S_{21} measurement.

The schematic of our test setup is shown in Figure 4-11. The probed laser sitting on a heat sink is assembled in a micro positioner. Light emitting from the cleaved facet is collected by a 20X objective. A collimated beam from a laser diode at 1310 nm is used to illuminate the facet of probed sample. A removable mirror is used to direct the laser emission to the infrared camera or the high speed photodetector. The facet with cleaved waveguides will be imaged on the camera for the alignment before testing. DC from laser diode driver (LDX-3500) and RF signal from Port 1 of vector network analyzer (Aglient 8720D) are combined by a bias tee, then are injected into the probed laser through a picoprobe. The figure of our picoprobe is shown in Figure 4-12, where the tips of ground and signal are separated by 200 μm, corresponding to the distance between n-contact and p-contact on top of the sample. A high-speed photodetector (Newport 818-BB-35) is connected to the VNA. In the measurement, VNA detects the S_{21} between two ports, and a multimeter is monitoring the DC component from the photodetector at the same time.

Figure 4-12 The picoprobe for injecting RF signal to chips.

In the measurement, we first pump the straight bus waveguide as a semiconductor optical amplifier. Since the devices are symmetric, leaving another long straight part unpumped, the bus waveguide cannot lase during the measurement due to a lack of optical feedback. With the increase of injected current to the ring, a laser emission was observed on the camera, as shown in Figure 4-13. The spectrum evolution was verified and shown in Figure 4-13, exhibiting a threshold around 27 mA, multi-longitude modes slightly above the threshold, and single mode emission with a higher current injection. From Figure 4-13, the splitting on the spectrum is 2 nm, corresponding to the free spectrum range of a ring resonator with a radius of 50 μm, where $\nu_{FSR} = c/2\pi Rn$.

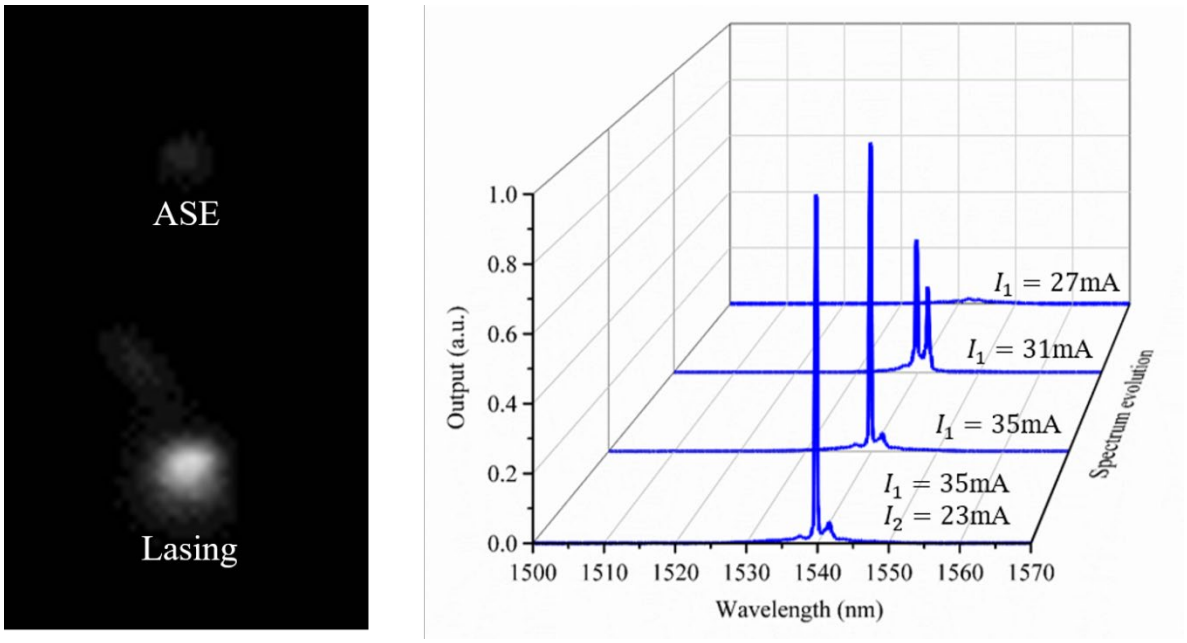

Figure 4-13 Laser emission and evolution of spectrum.

The *LIV* curves of two coupled rings are measured separately and are shown in Figure 4-14. Both ring lasers show threshold currents around 27 mA. With the increase of injected current above 40 mA, both ring exhibit a tendency of saturation. It can be explained by the confinement factor.

In our design, we increase the optically confinement to reduce the bending loss. Therefore, the photon density is higher compared to the ridge structure at the same pump level. Also, the thermal conductivity is not good enough because the waveguide is narrow and almost embedded into BCB which has a great thermal resist compared to the semiconductor material. From the *IV* curve, the resistance of probed laser is measured to be $R_{ld} = R_{total} - R_{load} = 15\Omega - 10\Omega = 5\Omega$, which exhibits a good ohmic contact on the metal-semiconductor interface. The relatively high threshold current and applied DC voltage imply a high surface recombination, though a sulfide surface passivation was employed.

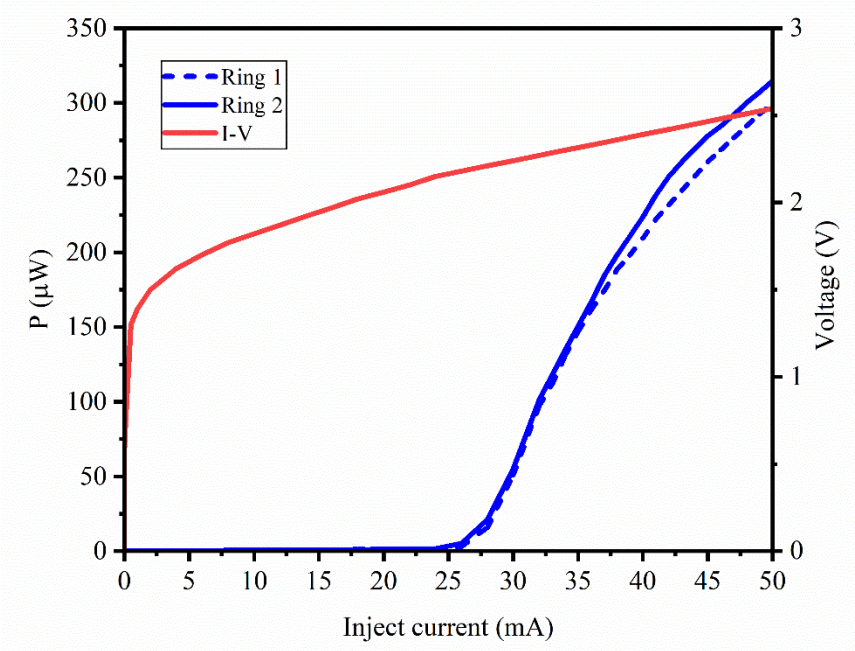

Figure 4-14 *LIV* curves of two coupled microring lasers that are testes individually.

4.8. Measurement of modulation responses

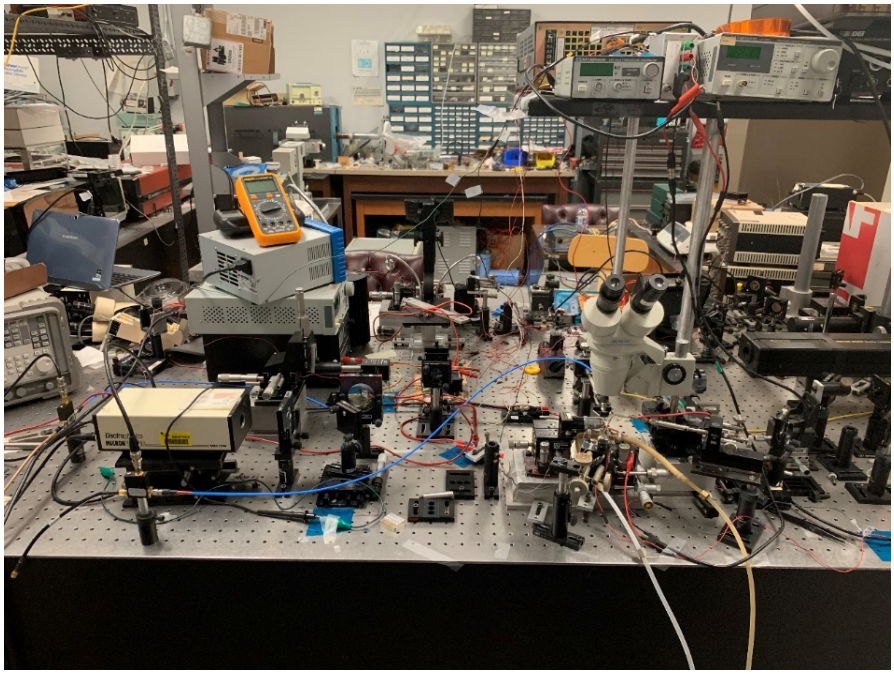

Figure 4-15 The measurement station of laser modulation responses

The S_{21} of the probe-laser-PD system is directly measured by VNA then normalized by the free running response in order to compensate the stopband of VNA at lower frequency. The bandwidths of picoprobe and photodetector are 40 GHz and 15 GHz, respectively. Thus any roll-off below 15 GHz can be attributed to the laser diode. The frequency response of a ring laser with an injection current of 35 mA is shown in Figure 4-16, which exhibits a bandwidth of 2.2 GHz (black curve). With the increase of pumping current on ring 2, the modulation bandwidth broadens to 3 GHz (red curve) then to 3.6 GHz (blue curve). The ring 2 is pumped lower or closed to its threshold in order to avoid the clamp of the gain. Therefore, the gain-loss contrast can be directly modified by the difference of injection currents between two rings. DC component from the photodetector is separated by a bias tee and monitored by a voltmeter during the measurement for

obtaining the averaged photo density of the ring 1. When I_2 increases, we adjust I_1 slightly to make sure the photon density keep invariant. By tuning the gain-loss contrast between two coupled microring cavities, a modulation bandwidth enhancement of 1.63 times was observed without increasing photon density of ring 1. The spectrum for the case of blue curve is shown in Figure 4-13, without an obvious change compared to the single ring.

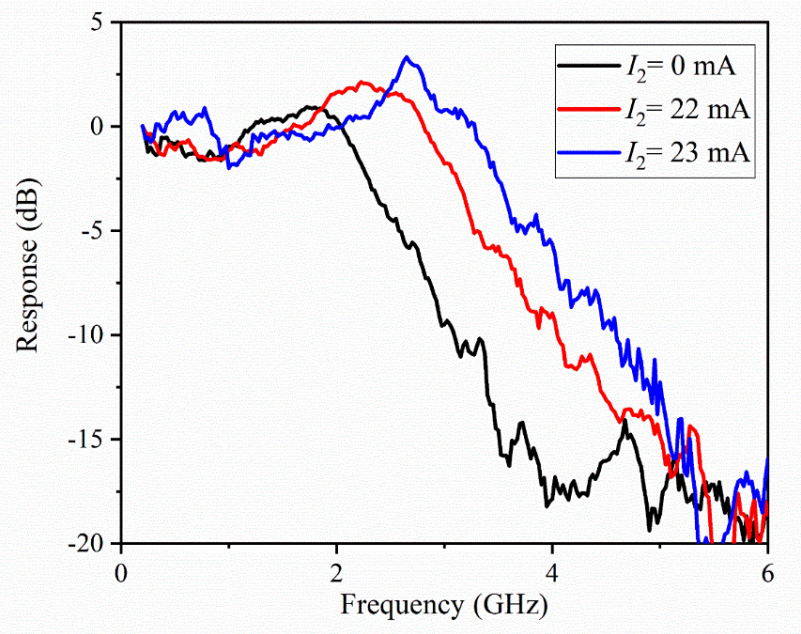

Figure 4-16 Modulation responses with various pump ratios between two rings.

4.9. Conclusion

We design and fabricate the microring laser system on a InAlGaAs MQW medium. The laser with a radius of 50 μm can realize CW operation at room temperature with a threshold current at 27 mA. By pumping the primary ring at a specific level, its modulation responses can be tuned by the injection current of the second ring. And the modulation bandwidth can be broadened by up to 1.63 times without increasing the photon density of the probed ring laser. We experimentally

verified the gain-loss contrast between two identical coupled cavities can be used as a new degree of freedom to enhance the modulation bandwidth.

CHAPTER 5 : CONCLUSION

In conclusion, we have investigated two novel mechanisms of enhancing the modulation bandwidth of semiconductor lasers. We first experimentally verify the high speed performances of nanolasers with strong cavity enhanced spontaneous emission, achieved by a subwavelength metal-clad cavity. The spontaneous emission coupling factor is 0.193, which is few order greater than conventional laser diodes. By employing a point-by-point measurement, a modulation bandwidth of 9 GHz was observed at a pump level as low as 0.25 mW/μm^2. A figure of merit, D-factor, is measured to be 107.5 GHz/mW$^{1/2}$, which is an order of magnitude larger than any other semiconductor lasers.

Another scheme of improving direct modulation performance is realized by gain-loss contrast. By coupling the laser cavity to another identical entity with a tunable loss, a bandwidth broadening of more than 2 times is theoretically demonstrated on the coupled microring laser system. This improvement is attributed to appearance of another pole of response functions due to the optical coupling. This expected modulation enhancement was then verified by fabricating electrically pumped microring lasers on InAlGaAs MQW EPI wafer. The coupled ring laser with a radius of 50 μm can operate in CW mode at room temperature with a threshold current of 27 mA on each ring. The modulation frequency response is directly measured by a VNA. By tuning the injection current on the lossy ring while keeping the output power of the gain ring at the same value, a bandwidth broadening of 1.63 times was experimentally observed. This enhancement is attributed to the gain-loss contrast instead of the photon density. We believe these two novel

mechanisms of broadening the modulation bandwidth could help pave the way for the next generation of on-chip light sources.

LIST OF REFERENCES

1.D. A. Miller, "Device requirements for optical interconnects to silicon chips," Proceedings of the IEEE **97**, 1166-1185 (2009).

2.D. A. Miller, "Optical interconnects to electronic chips," Applied optics **49**, F59-F70 (2010).

3.Y. Suematsu, S. Arai, and F. Koyama, "Dynamic-single-mode lasers," Optica Acta: International Journal of Optics **32**, 1157-1173 (1985).

4.T. Simpson, J. Liu, and A. Gavrielides, "Bandwidth enhancement and broadband noise reduction in injection-locked semiconductor lasers," IEEE Photonics Technology Letters **7**, 709-711 (1995).

5.R. Lang, "Injection locking properties of a semiconductor laser," IEEE Journal of Quantum Electronics **18**, 976-983 (1982).

6.J. D. Ralston, S. Weisser, I. Esquivias, E. C. Larkins, J. Rosenzweig, P. J. Tasker, and J. Fleissner, "Control of differential gain, nonlinear gain and damping factor for high-speed application of GaAs-based MQW lasers," IEEE Journal of Quantum Electronics **29**, 1648-1659 (1993).

7.C. Chen, K. L. Johnson, M. Hibbs-Brenner, and K. D. Choquette, "Push-pull modulation of a composite-resonator vertical-cavity laser," IEEE Journal of Quantum Electronics **46**, 438-446 (2010).

8.Y. Kominis, K. D. Choquette, A. Bountis, and V. Kovanis, "Antiresonances and Ultrafast Resonances in a Twin Photonic Oscillator," IEEE Photonics Journal **11**, 1-9 (2019).

9.D. M. Grasso, D. K. Serkland, G. M. Peake, K. M. Geib, and K. D. Choquette, "Direct modulation characteristics of composite resonator vertical-cavity lasers," IEEE Journal of Quantum Electronics **42**, 1248-1254 (2006).

10.T. Suhr, N. Gregersen, K. Yvind, and J. Mørk, "Modulation response of nanoLEDs and nanolasers exploiting Purcell enhanced spontaneous emission," Optics express **18**, 11230-11241 (2010).

11.H. Altug, D. Englund, and J. Vučković, "Ultrafast photonic crystal nanocavity laser," Nature Physics **2**, 484 (2006).

12.C.-Y. A. Ni and S. L. Chuang, "Theory of high-speed nanolasers and nanoLEDs," Optics Express **20**, 16450-16470 (2012).

13.D. M. Kuchta, A. V. Rylyakov, F. E. Doany, C. L. Schow, J. E. Proesel, C. W. Baks, P. Westbergh, J. S. Gustavsson, and A. Larsson, "A 71-Gb/s NRZ modulated 850-nm VCSEL-based optical link," IEEE Photonics Technology Letters **27**, 577-580 (2015).

14.W. Hofmann and D. Bimberg, "VCSEL-based light sources—Scalability challenges for VCSEL-based multi-100-Gb/s Systems," IEEE Photonics Journal **4**, 1831-1843 (2012).

15.M. P. Nezhad, A. Simic, O. Bondarenko, B. Slutsky, A. Mizrahi, L. Feng, V. Lomakin, and Y. Fainman, "Room-temperature subwavelength metallo-dielectric lasers," Nature Photonics **4**, 395 (2010).

16.M. T. Hill, Y.-S. Oei, B. Smalbrugge, Y. Zhu, T. De Vries, P. J. Van Veldhoven, F. W. Van Otten, T. J. Eijkemans, J. P. Turkiewicz, and H. De Waardt, "Lasing in metallic-coated nanocavities," Nature Photonics **1**, 589 (2007).

17.J. H. Lee, M. Khajavikhan, A. Simic, Q. Gu, O. Bondarenko, B. Slutsky, M. P. Nezhad, and Y. Fainman, "Electrically pumped sub-wavelength metallo-dielectric pedestal pillar lasers," Optics Express **19**, 21524-21531 (2011).

18.S. S. Deka, S. H. Pan, Q. Gu, Y. Fainman, and A. J. O. l. El Amili, "Coupling in a dual metallo-dielectric nanolaser system," Optics Letters **42**, 4760-4763 (2017).

19.M. Khajavikhan, A. Simic, M. Katz, J. Lee, B. Slutsky, A. Mizrahi, V. Lomakin, and Y. Fainman, "Thresholdless nanoscale coaxial lasers," Nature **482**, 204 (2012).

20.J. B. Khurgin and G. Sun, "Comparative analysis of spasers, vertical-cavity surface-emitting lasers and surface-plasmon-emitting diodes," Nature Photonics **8**, 468 (2014).

21.E. K. Lau, A. Lakhani, R. S. Tucker, and M. C. Wu, "Enhanced modulation bandwidth of nanocavity light emitting devices," Optics Express **17**, 7790-7799 (2009).

22.İ. Baştürk, Y. Chen, and M.-S. J. P. C. Alouini, "Energy-efficient communication for user-relay aided cellular networks with OFDMA," Physical Communications **33**, 153-164 (2019).

23.O. Anton, G. Vaschenko, D. Patel, J. M. Pikal, and C. S. Menoni, "Small Signal Frequency Response of laser diodes using a femtosectond frequency comb," in *Semiconductor Lasers and*

Optical Amplifiers for Lightwave Communication Systems, (International Society for Optics and Photonics, 2002), 95-103.

24.M. A. Newkirk and K. J. Vahala, "Parasitic-free measurement of the fundamental frequency response of a semiconductor laser by active-layer photomixing," Applied Physics Letters **52**, 770-772 (1988).

25.C. Su, J. Eom, C. Lange, C. Kim, R. Lauer, W. C. Rideout, and J. S. LaCourse, "Characterization of the dynamics of semiconductor lasers using optical modulation," IEEE Journal of Quantum Electronics **28**, 118-127 (1992).

26.K. G. Makris, R. El-Ganainy, D. Christodoulides, and Z. H. Musslimani, "Beam dynamics in P T symmetric optical lattices," Physical Review Letters **100**, 103904 (2008).

27.R. El-Ganainy, K. G. Makris, M. Khajavikhan, Z. H. Musslimani, S. Rotter, and D. N. Christodoulides, "Non-Hermitian physics and PT symmetry," Nature Physics **14**, 11 (2018).

28.M. P. Hokmabadi, N. S. Nye, R. El-Ganainy, D. N. Christodoulides, and M. Khajavikhan, "Supersymmetric laser arrays," Science **363**, 623-626 (2019).

29.G. Harari, M. A. Bandres, Y. Lumer, M. C. Rechtsman, Y. D. Chong, M. Khajavikhan, D. N. Christodoulides, and M. Segev, "Topological insulator laser: theory," Science **359**(2018).

30.M. A. Bandres, S. Wittek, G. Harari, M. Parto, J. Ren, M. Segev, D. N. Christodoulides, and M. Khajavikhan, "Topological insulator laser: Experiments," Science **359**(2018).

31.Z. Lin, H. Ramezani, T. Eichelkraut, T. Kottos, H. Cao, and D. N. Christodoulides, "Unidirectional invisibility induced by P T-symmetric periodic structures," Physical Review Letters **106**, 213901 (2011).

32.A. Regensburger, C. Bersch, M.-A. Miri, G. Onishchukov, D. N. Christodoulides, and U. Peschel, "Parity–time synthetic photonic lattices," Nature **488**, 167 (2012).

33.L. Feng, Y.-L. Xu, W. S. Fegadolli, M.-H. Lu, J. E. Oliveira, V. R. Almeida, Y.-F. Chen, and A. Scherer, "Experimental demonstration of a unidirectional reflectionless parity-time metamaterial at optical frequencies," Nature Materials **12**, 108 (2013).

34.J. Wiersig, "Enhancing the sensitivity of frequency and energy splitting detection by using exceptional points: application to microcavity sensors for single-particle detection," Physical Review Letters **112**, 203901 (2014).

35.H. Hodaei, A. U. Hassan, S. Wittek, H. Garcia-Gracia, R. El-Ganainy, D. N. Christodoulides, and M. Khajavikhan, "Enhanced sensitivity at higher-order exceptional points," Nature **548**, 187 (2017).

36.W. Chen, Ş. K. Özdemir, G. Zhao, J. Wiersig, and L. Yang, "Exceptional points enhance sensing in an optical microcavity," Nature **548**, 192 (2017).

37.J. Doppler, A. A. Mailybaev, J. Böhm, U. Kuhl, A. Girschik, F. Libisch, T. J. Milburn, P. Rabl, N. Moiseyev, and S. Rotter, "Dynamically encircling an exceptional point for asymmetric mode switching," Nature **537**, 76 (2016).

38.H. Xu, D. Mason, L. Jiang, and J. Harris, "Topological energy transfer in an optomechanical system with exceptional points," Nature **537**, 80 (2016).

39.A. U. Hassan, B. Zhen, M. Soljačić, M. Khajavikhan, and D. N. Christodoulides, "Dynamically encircling exceptional points: exact evolution and polarization state conversion," Physical Review Letters **118**, 093002 (2017).

40.H. Hodaei, M.-A. Miri, M. Heinrich, D. N. Christodoulides, and M. Khajavikhan, "Parity-time–symmetric microring lasers," Science **346**, 975-978 (2014).

41.L. Feng, Z. J. Wong, R.-M. Ma, Y. Wang, and X. Zhang, "Single-mode laser by parity-time symmetry breaking," Science **346**, 972-975 (2014).

42.H. Hodaei, A. U. Hassan, J. Ren, W. E. Hayenga, M.-A. Miri, D. N. Christodoulides, and M. Khajavikhan, "Design Considerations for Single-Mode Microring Lasers Using Parity-Time-Symmetry," IEEE Journal of Selected Topics in Quantum Electronics **22**, 12-18 (2016).

43.Y. Kominis, K. D. Choquette, A. Bountis, and V. Kovanis, "Exceptional points in two dissimilar coupled diode lasers," Applied Physics Letters **113**, 081103 (2018).

44.E. Zeeb, B. Moller, C. Reiner, M. Ries, T. Hackbarth, and K. J. Ebeling, "Planar proton implanted VCSEL's and fiber-coupled 2-D VCSEL arrays," IEEE Journal of Selected Topics in Quantum Electronics **1**, 616-623 (1995).

45.C. J. Chang-Hasnain, "Tunable vcsel," IEEE Journal of Selected Topics in Quantum Electronics **6**, 978-987 (2000).

46.M. Agio and D. M. Cano, "The Purcell factor of nanoresonators," Nature Photonics **7**, 674-675 (2013).

47.Ş. K. Özdemir, J. Zhu, L. He, and L. Yang, "Estimation of Purcell factor from mode-splitting spectra in an optical microcavity," Physical Review A **83**, 033817 (2011).

48.T. Baba and D. Sano, "Low-threshold lasing and Purcell effect in microdisk lasers at room temperature," IEEE Journal of Selected Topics in Quantum Electronics **9**, 1340-1346 (2003).

49.A. Mizrahi, V. Lomakin, B. A. Slutsky, M. P. Nezhad, L. Feng, and Y. Fainman, "Low threshold gain metal coated laser nanoresonators," Optics Letters **33**, 1261-1263 (2008).

50.Q. Gu, B. Slutsky, F. Vallini, J. S. Smalley, M. P. Nezhad, N. C. Frateschi, and Y. Fainman, "Purcell effect in sub-wavelength semiconductor lasers," Optics Express **21**, 15603-15617 (2013).

51.K. Ding, M. Hill, Z. Liu, L. Yin, P. Van Veldhoven, and C.-Z. Ning, "Record performance of electrical injection sub-wavelength metallic-cavity semiconductor lasers at room temperature," Optics Express **21**, 4728-4733 (2013).

52.K. Ding, Z. Liu, L. Yin, H. Wang, R. Liu, M. T. Hill, M. J. Marell, P. J. Van Veldhoven, R. Nötzel, and C.-Z. Ning, "Electrical injection, continuous wave operation of subwavelength-metallic-cavity lasers at 260 K," Applied Physics Letters **98**, 231108 (2011).

53.J. C. Norman, D. Jung, Y. Wan, and J. E. Bowers, "Perspective: The future of quantum dot photonic integrated circuits," APL Photonics **3**, 030901 (2018).

54.A. Y. Liu, C. Zhang, J. Norman, A. Snyder, D. Lubyshev, J. M. Fastenau, A. W. Liu, A. C. Gossard, and J. E. Bowers, "High performance continuous wave 1.3 μ m quantum dot lasers on silicon," Applied Physics Letters **104**, 041104 (2014).

55.A. Y. Liu, S. Srinivasan, J. Norman, A. C. Gossard, and J. E. Bowers, "Quantum dot lasers for silicon photonics," Photonics Research **3**, B1-B9 (2015).

56.Y. Wan, J. Norman, Q. Li, M. Kennedy, D. Liang, C. Zhang, D. Huang, Z. Zhang, A. Y. Liu, and A. Torres, "1.3 μm submilliamp threshold quantum dot micro-lasers on Si," Optica **4**, 940-944 (2017).

57.Y. Wan, Q. Li, A. Y. Liu, A. C. Gossard, J. E. Bowers, E. L. Hu, and K. M. Lau, "Temperature characteristics of epitaxially grown InAs quantum dot micro-disk lasers on silicon for on-chip light sources," Applied Physics Letters **109**, 011104 (2016).

58.W. E. Hayenga, H. Garcia-Gracia, H. Hodaei, Y. Fainman, and M. Khajavikhan, "Metallic coaxial nanolasers," Advances in Physics: X **1**, 262-275 (2016).

59.J.-M. Gérard and B. J. J. o. l. t. Gayral, "Strong Purcell effect for InAs quantum boxes in three-dimensional solid-state microcavities," IEEE Journal of Lightwave Technology **17**, 2089-2095 (1999).

60.M. Muller, W. Hofmann, T. Grundl, M. Horn, P. Wolf, R. D. Nagel, E. Ronneberg, G. Bohm, D. Bimberg, and M.-C. Amann, "1550-nm high-speed short-cavity VCSELs," IEEE Journal of Selected Topics in Quantum Electronics **17**, 1158-1166 (2011).

61.L. A. Coldren, S. W. Corzine, and M. L. Mashanovitch, *Diode lasers and photonic integrated circuits* (John Wiley & Sons, 2012), Vol. 218.

62.D. Tauber, G. Wang, R. Geels, J. Bowers, and L. J. A. p. l. Coldren, "Large and small signal dynamics of vertical cavity surface emitting lasers," Applied Physics Letters **62**, 325-327 (1993).

63.C. H. Lange, J. Eom, C. Su, J. Schlafer, and R. Lauer, "Measurement of intrinsic frequency response of semiconductor lasers using optical modulation," Electronics Letters **24**, 1131-1132 (1988).

64.M. Jammer, *The conceptual development of quantum mechanics* (McGraw-Hill New York, 1966).

65.C. M. Bender, S. Boettcher, and P. N. Meisinger, "PT-symmetric quantum mechanics," Journal of Mathematical Physics **40**, 2201-2229 (1999).

66.C. M. Bender, D. C. Brody, and H. F. Jones, "Extension of PT-symmetric quantum mechanics to quantum field theory with cubic interaction," Physical Review D **70**, 025001 (2004).

67.A. U. Hassan, H. Hodaei, M.-A. Miri, M. Khajavikhan, and D. N. Christodoulides, "Nonlinear reversal of the PT-symmetric phase transition in a system of coupled semiconductor microring resonators," Physical Review A **92**, 063807 (2015).

68.J. Ren, Y. G. Liu, M. Parto, W. E. Hayenga, M. P. Hokmabadi, D. N. Christodoulides, and M. Khajavikhan, "Unidirectional light emission in PT-symmetric microring lasers," Optics Express **26**, 27153-27160 (2018).

69.Z. Xu, D. Birkedal, M. Juhl, and J. M. Hvam, "Submonolayer InGaAs / GaAs quantum-dot lasers with high modal gain and zero-linewidth enhancement factor," Applied Physics Letters **85**, 3259-3261 (2004).

70.P. K. Kondratko, S.-L. Chuang, G. Walter, T. Chung, and N. Holonyak Jr, "Observations of near-zero linewidth enhancement factor in a quantum-well coupled quantum-dot laser," Applied Physics Letters **83**, 4818-4820 (2003).

71.E. H. Li, "Material parameters of InGaAsP and InAlGaAs systems for use in quantum well structures at low and room temperatures," Physica E: Low-dimensional systems and Nanostructures **5**, 215-273 (2000).

72.D. Chu, M. Chin, N. Sauer, Z. Xu, T. Chang, and S. Ho, "1.5-mu m InGaAs/InAlGaAs quantum-well microdisk lasers," IEEE Photonics Technology Letters **5**, 1353-1355 (1993).

73.B. E. Little, S. T. Chu, H. A. Haus, J. Foresi, and J.-P. Laine, "Microring resonator channel dropping filters," IEEE Journal of Lightwave Technology **15**, 998-1005 (1997).

74.X. Xu and Z. Wang, "Thermal conductivity enhancement of benzocyclobutene with carbon nanotubes for adhesive bonding in 3-D integration," IEEE Transactions on Components, Packaging and Manufacturing Technology **2**, 286-293 (2011).

75.J. Jaramillo-Fernandez, E. Chavez-Angel, R. Sanatinia, H. Kataria, S. Anand, S. Lourdudoss, and C. M. Sotomayor-Torres, "Thermal conductivity of epitaxially grown InP: experiment and simulation," CrystEngComm **19**, 1879-1887 (2017).

76.W. Zhu, G. Zheng, S. Cao, and H. He, "Thermal conductivity of amorphous SiO 2 thin film: a molecular dynamics study," Scientific reports **8**, 1-9 (2018).

77.X. Zhang and C. P. Grigoropoulos, "Thermal conductivity and diffusivity of free‐standing silicon nitride thin films," Review of Scientific Instruments **66**, 1115-1120 (1995).

78.C. Henry, R. Logan, and F. Merritt, "The effect of surface recombination on current in Al x Ga1− x As heterojunctions," Journal of Applied Physics **49**, 3530-3542 (1978).

79.M. Fukuda, "Current drift associated with surface recombination current in InGaAsP/InP optical devices," Journal of Applied Physics **59**, 4172-4176 (1986).

80.L. Abenante, "Simple analytical model for 2 k T current in forward-biased p-n junctions," Journal of Applied Physics **97**, 013703 (2005).

81.G. Reeves and H. Harrison, "Obtaining the specific contact resistance from transmission line model measurements," IEEE Electron Device Letters **3**, 111-113 (1982).